National Research Programme
„Cyber-physical systems, ontologies and biophotonics for safe&smart city and society”
(SOPHIS)

Project No.3

“BIOPHOTONICS: imaging, diagnostics and monitoring”

FINAL SCIENTIFIC REPORT

Riga

2017

Contents

List of abbreviations

RGB – red-green-blue system for color image acquisition

LED – light-emitting diode

CMOS - complementary metal–oxide–semiconductor, a structure used in digital image sensors

PPGI – photoplethysmography imaging, a technique for remote detection of skin blood pulsations; also abbreviated as rPPG (remote photoplethysmography)

EI – erythema index

CEA – visual assessment scale (from 1 to 4)

Introduction

Three main goals were defined for this project:

- To develop innovative technologies for capturing and processing of bio-object images
- To develop and approbate new, image-based methodologies of clinical diagnostics and monitoring.
- In collaboration with industrial partners, to approbate and implement the new developments in healthcare and related fields, to create basis for development of competitive products and services

In brief, 6 imaging technologies have been developed or improved in frame of this project, along with 6 developed and clinically approbated methodologies that were implemented in clinical praxis of two hospitals in Riga. The most significant results of the whole project are presented here; more details are given in the previous scientific reports (http://sophis.edi.lv) and in references listed at the end of this report.

1. Obtaining several monochromatic spectral images from a single digital color image: principles and applications for skin chromophore mapping and counterfeit banknote detection

Possibility for extraction of three monochromatic images of the target from a single RGB image data set under illumination simultaneously by 3 spectral lines was analyzed at the initial stage of this study. Monochromatic spectral images of the color targets were extracted from the RGB image data cube with respect of the RGB crosstalk correction, as described previously [1,2]. Measurements of various color targets at single- and three-wavelength laser illumination confirmed the versatility of this approach [3].

Single-snapshot skin chromophore mapping: the concept

The general concept of snapshot skin chromophore mapping at fixed wavelengths is illustrated at Fig.1. Let us suppose that RGB color image of a skin pathology spot, surrounded by healthy skin, is captured under illumination that comprises only three equal intensity spectral lines at wavelengths λ_1, λ_2 and λ_3.

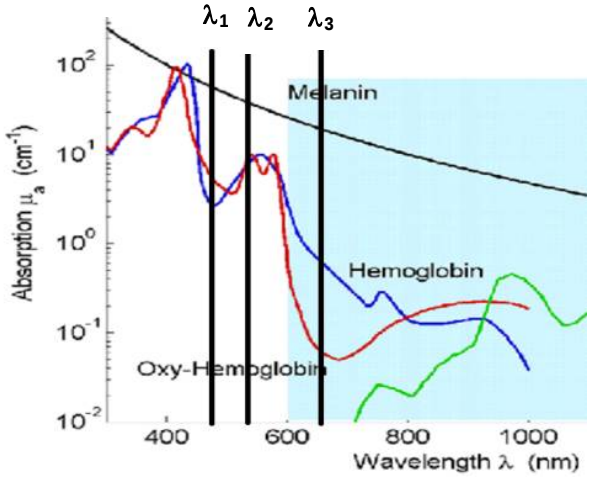

Fig. 1. Absorption of three main skin chromophores at three fixed wavelengths.

With respect to the spectral sensitivity of RGB image sensor and the cross-talk between its detection bands at the particular wavelengths, three monochromatic spectral images are extracted from the color image data set by the technique described above. The three chromophore skin model suggests that the dominant absorbers in skin at any of the fixed wavelengths λ_j (j = 1, 2, 3) are oxy-hemoglobin (further abbreviated by a), deoxy-hemoglobin (b) and melanin (c) – see the crossings of their absorption curves with the vertical lines at Fig.1. If the skin surface reflection is suppressed (e.g. by means of crossed polarizers), variations in chromophore composition would lead to changes of the diffusely reflected light intensities at each of the fixed wavelengths. Such variations in the pathology region relatively to the healthy skin can be estimated by measuring reflected light intensities from equally sized regions of interest in the pathology (I_j) and the adjacent healthy skin (I_{oj}). The ratios I_j/I_{jo} at each pixel or pixel's group of three monochromatic spectral images contain information on the concentration increase or decrease of all three regarded chromophores Δc_i (i = a, b, c), which can be further mapped over the whole image area.

Image Processing

The mentioned intensity changes due to absorption can be represented by the Beer–Lambert–Bouguer law:

$$\begin{cases} \ln\left(\frac{I_1}{I_{01}}\right) = -l_1\left(\Delta c_a \cdot \varepsilon_a(\lambda_1) + \Delta c_b \cdot \varepsilon_b(\lambda_1) + \Delta c_c \cdot \varepsilon_c(\lambda_1)\right) \\ \ln\left(\frac{I_2}{I_{02}}\right) = -l_2\left(\Delta c_a \cdot \varepsilon_a(\lambda_2) + \Delta c_b \cdot \varepsilon_b(\lambda_2) + \Delta c_c \cdot \varepsilon_c(\lambda_2)\right) \\ \ln\left(\frac{I_3}{I_{03}}\right) = -l_3\left(\Delta c_a \cdot \varepsilon_a(\lambda_3) + \Delta c_b \cdot \varepsilon_b(\lambda_3) + \Delta c_c \cdot \varepsilon_c(\lambda_3)\right) \end{cases} \quad (1),$$

where $\varepsilon_i(\lambda_j)$ - extinction coefficients of three regarded chromophores at three exploited wavelengths, l_j – absorption path length in skin at a particular wavelength. Chromophore concentration increase or decrease at each image pixel (or selected group of pixels) is found by solving the linear equation system (1) with abbreviated measured quantities $k_j = \ln(I_j/I_{jo})$:

$$\begin{aligned} \Delta c_a &= A_1 \cdot k_1 + A_2 \cdot k_2 + A_3 \cdot k_3 \\ \Delta c_b &= B_1 \cdot k_1 + B_2 \cdot k_2 + B_3 \cdot k_3 \\ \Delta c_c &= C_1 \cdot k_1 + C_2 \cdot k_2 + C_3 \cdot k_3 \end{aligned} \quad (2).$$

The coefficients A_j, B_j and C_j comprise numerical values of the corresponding chromophore extinction coefficients $\varepsilon_i(\lambda_j)$ and absorption path lengths l_j at the three exploited wavelengths. The respective extinction coefficients for oxy-hemoglobin, deoxy-hemoglobin and melanin for our working wavelengths 448nm, 532nm and 659nm are presented in Table 1.

Table 1. The extinction coefficients of three main skin chromophores [4,5] at three exploited wavelengths.

Chromophore	ε (448 nm) [1/mol.cm]	ε (532 nm) [1/mol.cm]	ε (659 nm) [1/mol.cm]
Melanin	1935	1170	541
Oxy-hemoglobin	67044	45400	320
Deoxy-hemoglobin	173320	41336	3227

Table 2. Optical properties of skin layers used in the simulations.

	λ, nm	μ_s, mm^{-1}	μ_a, mm^{-1}	*g*	*n*
Epidermis	659	20	0.20	0.90	1.36
	532	27	0.60	0.85	1.36
	448	33	1.0	0.84	1.36
Dermis	659	18	0.12	0.90	1.40
	532	22	0.30	0.85	1.40
	448	27	0.65	0.84	1.40
Subcutaneous tissues	659	7	0.07	0.80	1.40
	532	10	0.40	0.76	1.40
	448	14	0.70	0.75	1.40

The Beer–Lambert–Bouguer law is originally addressed to absorption of light beam passing through a slab of substance with thickness x. If this law is adapted to the diffusely remitted light geometry, slab thickness x has to be replaced by the mean path length l_j of the back-scattered photons inside the skin at a particular wavelength. To estimate the l_j values with respect to light scattering properties, Monte Carlo (MC) simulations in frame of the two-

layered skin model (epidermal and dermal layers followed by the infinite subcutaneous tissue layer) were performed. Optical parameters of the tissue layers for the considered wavelengths were averaged from a number of the available sources for typical Caucasian skin, see Table 2.

The simulations have been performed for various thicknesses of the epidermal layer (200, 150 and 100μm) and dermis of 1800μm. In the simulations, uniform illumination beam with the diameter of 50 mm has been accounted. The diffusely backscattered (remitted) photons were collected from the same area accounting for the aperture angle of 10 deg. As the outcome, the distributions of the detected photons over their total path length and maximal penetration depth were generated. The simulation results for skin with epidermal thickness of 200 μm are presented in Fig. 2.

MC simulations showed increased photon penetration depth and total path length with growing wavelength, the mean path length of the remitted photons being approximately 4 to 5 times longer than their average penetration depth. The MC calculation results are presented in Table 3. One can see that the mean path length of photons in skin at a fixed wavelength is quite insensitive (<10%) to the twofold increase/decrease of the epidermal thickness. Consequently, different skin epidermal thicknesses should not seriously influence the data obtained by the proposed technique.

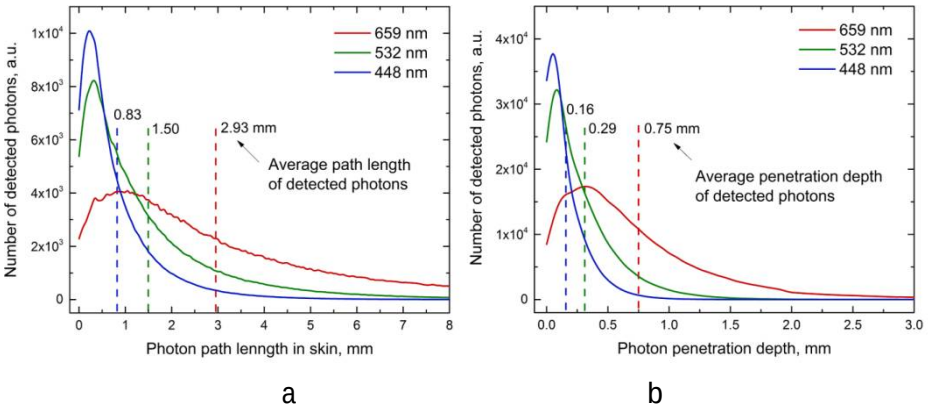

Fig. 2. Monte Carlo simulated distributions of the detected photons over their total path length (a) and penetration depth (b) inside the skin (thickness of epidermis - 200 μm) for three exploited wavelengths.

Table 3. MC-estimated penetration depths and path length in skin of the remitted photons

Wavelength, nm	Epidermal thickness, mm	Mean penetration depth, mm	Mean path length in skin, mm	The calculated ratio factor
448	0.20	0.16	0.83	5.19
	0.15	0.17	0.88	5.18
	0.10	0.18	0.92	5.11
532	0.20	0.29	1.50	5.17
	0.15	0.31	1.57	5.06
	0.10	0.32	1.64	5.13
659	0.20	0.75	2.93	3.91
	0.15	0.76	2.95	3.88
	0.10	0.76	2.98	3.92

The prototype devices

A compact smartphone-compatible three wavelength illuminator has been designed, assembled and tested in the laboratory and clinics. Fig.3 shows the design details (left) and outlook of operating prototype with smartphone on it (right). Flat ring-shaped laser diffuser [6] ensures uniform three wavelength illumination of the round target area with diameter 40 mm. The illumination wavelengths 448 nm, 532 nm and 659 nm are emitted by three pairs of

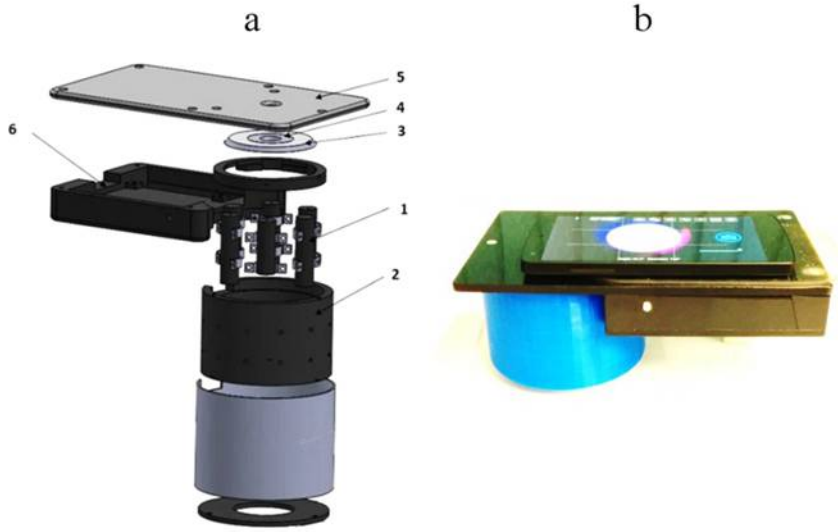

Fig.3. Design scheme of the 3-wavelength laser add-on illuminator (**a**) and the mobile prototype with smartphone on it (**b**): 1—laser modules (3 pairs, 448-532-659nm), 2—shielding cylinder, 3—collector of laser beams, 4—flat ring-shaped diffuser of laser light, 5—sticky platform for the smartphone, 6—electronics compartment.

compact 20 mW power laser modules (models *PGL-DF-450nm-20mW-15011564, PGL-VI-1-532nm-20mW-15030443* and *PGL-DF-655nm-20mW-150302232* from Changchun New Industries Optoelectronics Tech. Co., Ltd., Changchun, China). Laser modules (1, Figure 3a—showing three out of six) of each equal-wavelength pair are mounted at opposite sides on the internal wall of a hollow 3D-printed plastic shielding cylinder 2; the round bottom opening of this cylinder is in contact with skin and forms the field of view for the smartphone camera, situated 80 mm apart. All six coaxial laser beams are pointed to the 45-degree conical reflecting edge of a Plexiglass transparent disc 3 (beam collector); after reflections they are turned radial towards the internal ring-shaped flat milky-Plexiglas diffuser 4. In result, the flat diffuser 4 evenly illuminates the 65 mm distant skin target area simultaneously by the three laser wavelengths.

The smartphone is placed on flat sticky platform 5 with a round window for the smartphone rear camera, co-aligned with the internal opening of the diffuser 4. The round camera window is covered by a film polarizer; another film with orthogonal direction of polarization covers the diffuser 4 from bottom, so avoiding detection of skin surface-reflected light by the smartphone camera. We used a model *Google Nexus5* smartphone comprising an 8Mpx *SONY IMX179* image sensor with known RGB-sensitivities; spatial resolution of the imaging system was better than 0.1 mm.

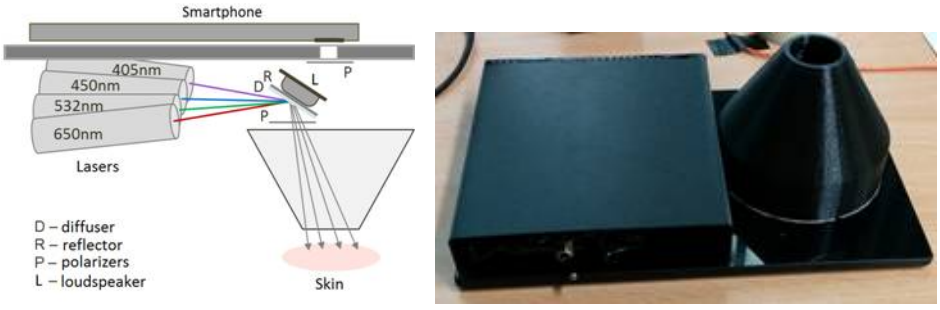

(**a**) (**b**)

Fig. 4. Design scheme (**a**) and outlook (**b**) of the prototype device for hand-switchable 4-wavelengths skin illumination.

The single-snapshot RGB technique is not applicable for express-mapping of more than three skin chromophores. We proposed and patented the double-snapshot approach [7] for fast obtaining 4, 5 or 6 monochromatic images. This concept has been implemented in a model device comprising switchable four laser illuminator and a smartphone. Fig. 4 shows the design scheme and outlook of a smartphone add-on illuminator intended for mapping of four skin chromophores, e.g., melanin, oxy-hemoglobin, deoxy-hemoglobin and bilirubin. Two of the laser modules can be manually switched on and off, so providing two sets of 3-wavelengths illumination (405, 532, 650 nm and 450, 532, 650 nm). Four rechargeable AA-type batteries are used for power supply. Relatively uniform illumination of round skin spot (dia. 18 mm) is provided by an advanced optical design which also reduces laser speckle artefacts – this solution was recently patented [8].

Besides, a portable self-sustained automatically switchable 5-wavelength (405, 448, 532, 659, 842 nm) laser illuminator of similar design, additionally equipped with own CMOS camera (NIR sensitive), Rasberry Pi3 processing unit and 3.5' touch screen, has been assembled (Fig.5). Two RGB snapshots are taken: first when 405, 532 and 659 nm wavelength lasers are switched on and second when 448, 532 and 842 nm wavelength lasers are switched on.

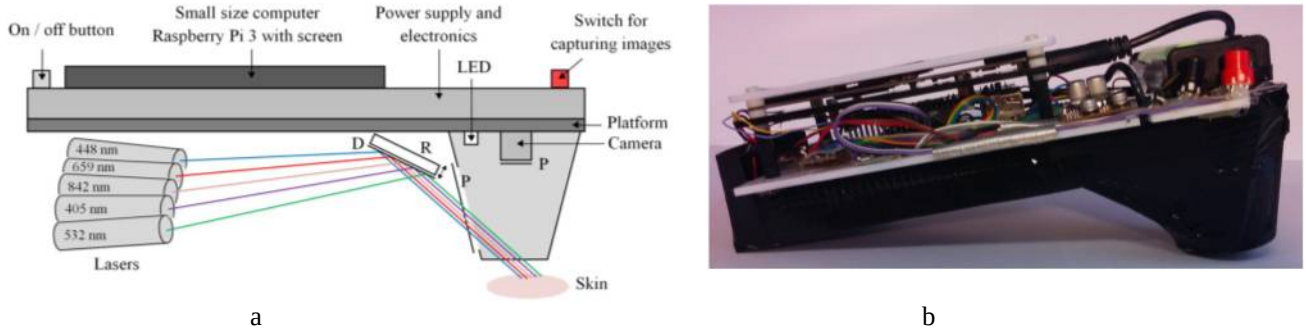

a b

Fig. 5. Design scheme (**a**) and outlook (**b**) of the 1st prototype imaging device with automatically switchable 5-wavelengths skin illumination: R – reflector, D – diffuser, P – polarizers.

-

–

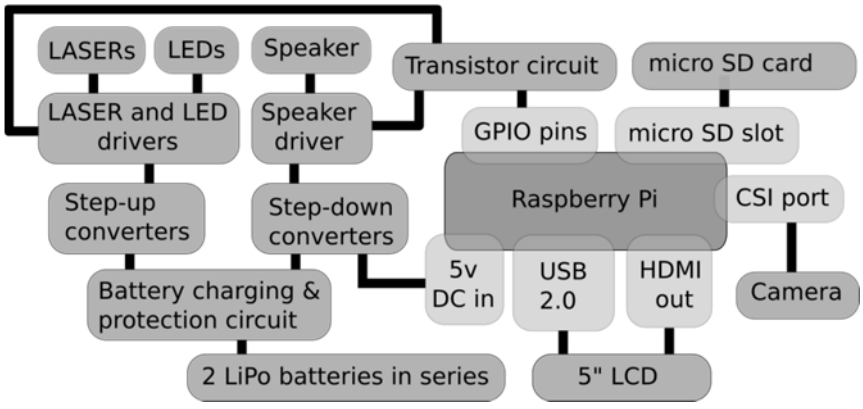

Fig. 6. Functional scheme of the 2nd prototype for obtaining 5 monochromatic images.

The cornerstone of the device is the Raspberry Pi computer. It captures images with camera module comprising NIR-sensitive OmniVision OV5647 image sensor and saves the images to microSD card that also holds OS and of the device. 5 different wavelength laser diodes (wavelengths 405nm, 450nm, 520nm, 660nm, 850nm) where used to illuminate skin; extra white LED illumination ensured pointing of camera to the region of interest and capturing of RGB image of the diseased skin area. To decrease the effects of speckle formation, a speaker was

attached to the diffuser and vibrated at about 400Hz. Drivers ensured proper functioning of lasers, white LED and microphone. Each driver worked at different specific voltage, so a switching mode power supply for each driver and individual control was provided. The Raspberry Pi was not able to deliver power demands for the drivers from its GPIO pins, so a transistor circuit was used. All of the power to switching power regulators (which power drivers and Raspberry Pi itself) came from two 5Ah lithium-polymer batteries in series. An appropriate charging and protection circuit was added to ensure safety. To relay image identification and to see what the camera is pointing to, a LCD screen was connected via HDMI connection and powered via USB. Two External pushbutton switches were added for convenience - one for image capturing and another for power control. The Raspberry Pi device had a version of Raspbian operating system installed. On bootup it launched Pyhon script that held the necessary information for device to work properly.

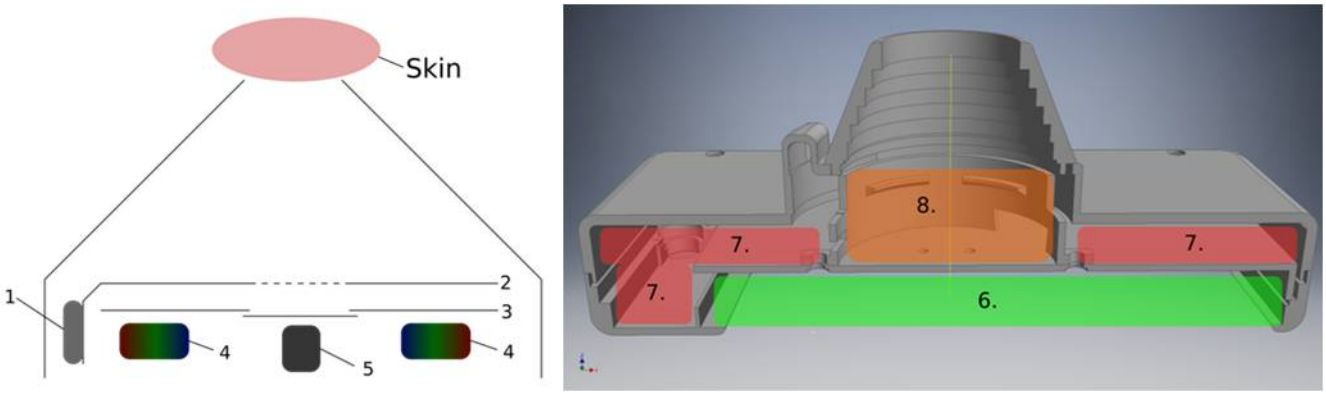

Fig. 7. Design scheme of optical system (left) and half section design view (right) of the 2nd prototype device: 1 – loudspeaker, 2 – diffuser, 3 – cross-oriented polarizers, 4 – illumination ring with 4x5 wavelength laser diodes and white LED, 5 – camera with OmniVision OV5647 sensor, 6 - 5" LCD touch screen and batteries, 7 - Raspberry Pi, control and power management circuits, 8 – optical system.

Fig. 8. The front and rear view of the 2nd prototype for obtaining 5 monochromatic images.

Results of the clinical measurements

The mobile smartphone and 3-wavelength illuminator system passed preliminary clinical tests under approval of the local ethics committee with written consent of 12 white skin (photo-types 1, 2) patients - 3 males and 9 females, 22-64 years old. Altogether 33 vascular and pigmented skin lesions were examined, including 21 pigmented nevi, 6 seborrheic keratosis and 6 hemangiomas; all mentioned skin malformations were diagnosed by an experienced dermatologist. The main goal of clinical measurements was to check if the above-described hardware and software can provide physiologically feasible information on already diagnosed skin malformations in terms of increased-decreased contents of the three regarded chromophores. Statistical quantitative analysis of skin malformations at this stage of development was not planned.

The patient measurement protocol included the following steps:

1) Standard dermatology procedure to diagnose the skin pathology;
2) Brief introduction to the patient about the new technology and the device;
3) Written consent of patient to participate;
4) Capture of calibration image of grey color reference under 3-wavelength illumination;
5) Adjustment of the device on the examined skin pathology and capturing its image under 3-wavelength illumination;
6) Repeated capture of the grey color reference image under 3-wavelength illumination.

The recorded pathology images were further processed by PC using the above-described algorithm. Reference images taken before and after the pathology image were compared to make sure that illumination conditions during the procedure have not changed. Gray reference (instead of white) was selected to avoid over-exposure of the image sensor.

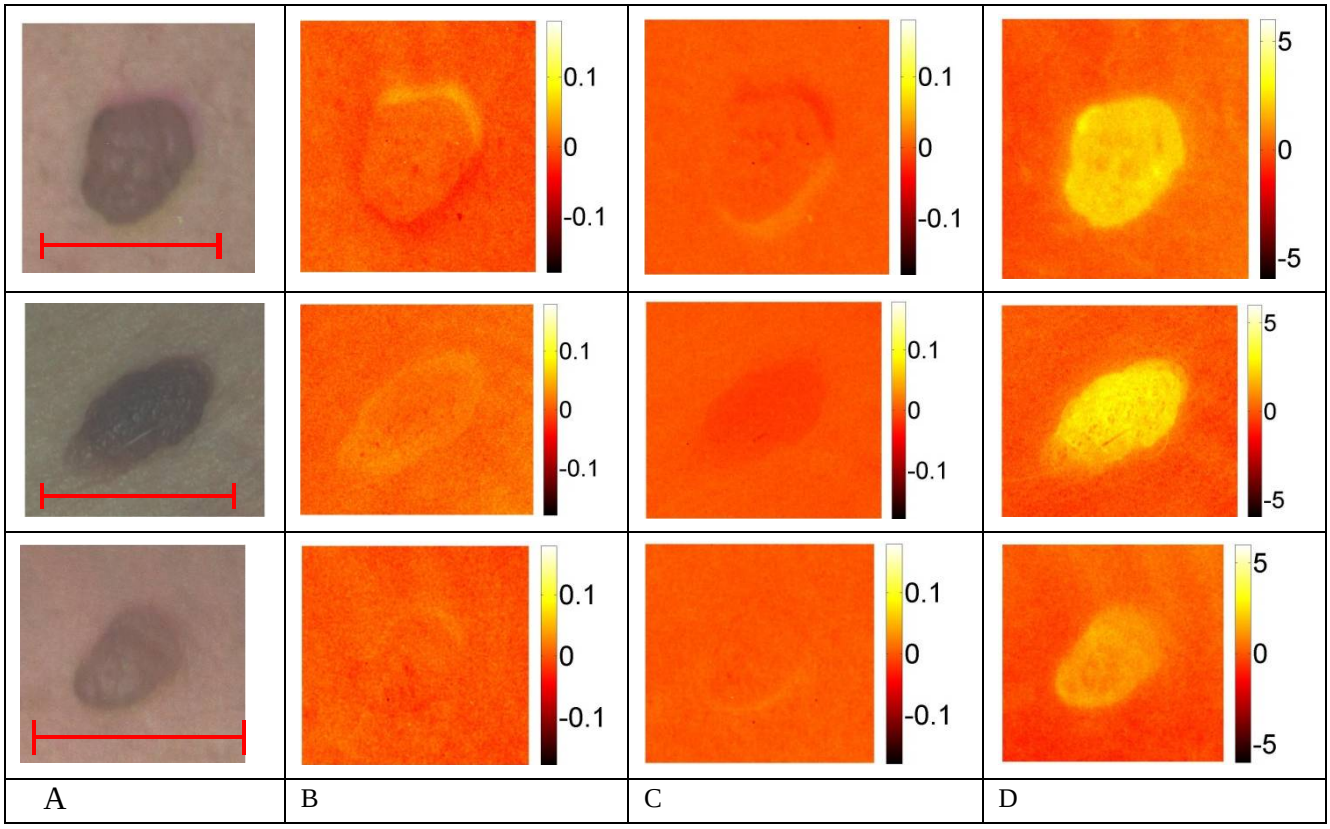

Fig.9. RGB image (A, scale bar 5 mm) and the corresponding maps representing chromophore concentration changes for three cases of pigmented nevi: B – oxy-hemoglobin, C – deoxy-hemoglobin, D – melanin. Units of the color scale – milimoles [mM].

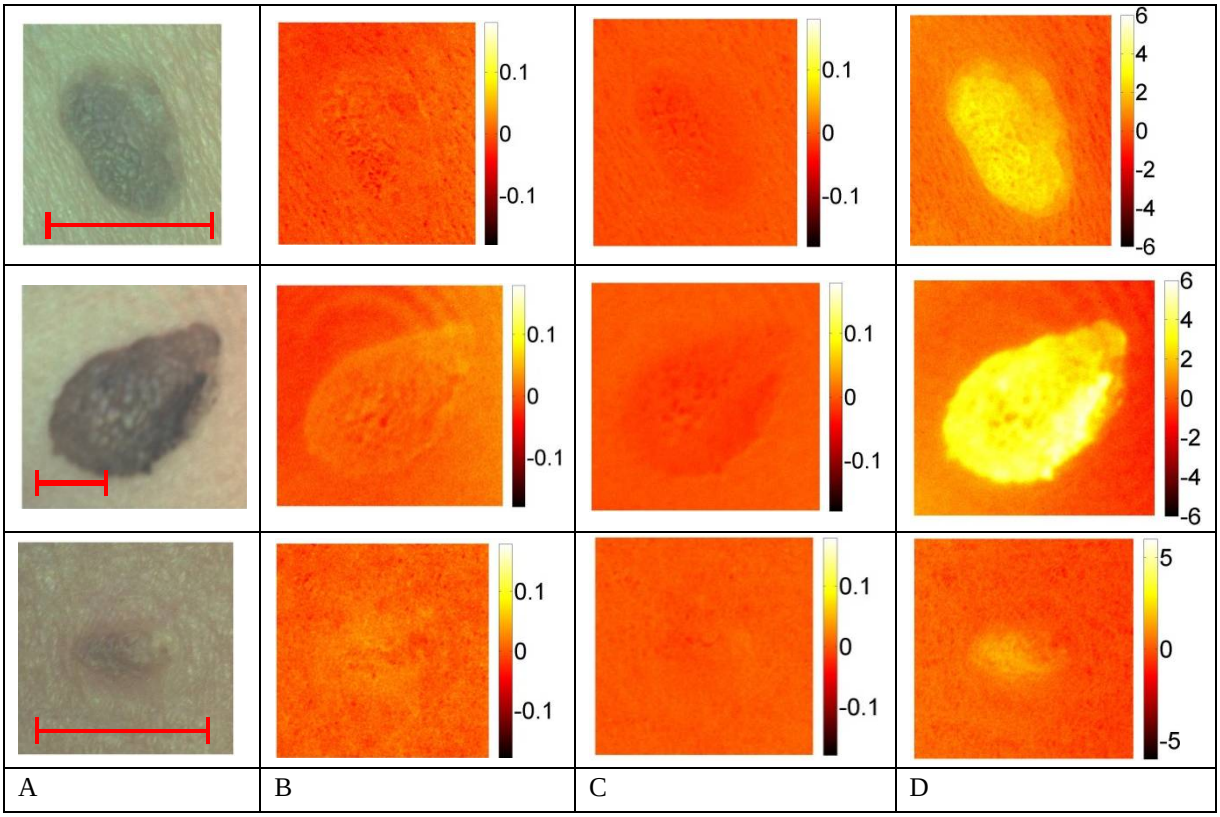

Fig.10. RGB image (A, scale bar 5 mm) and the corresponding maps representing chromophore concentration changes for three cases of pigmented seborrheic keratosis: B – oxy-hemoglobin, C – deoxy-hemoglobin, D – melanin. Units of color scale – milimoles [mM].

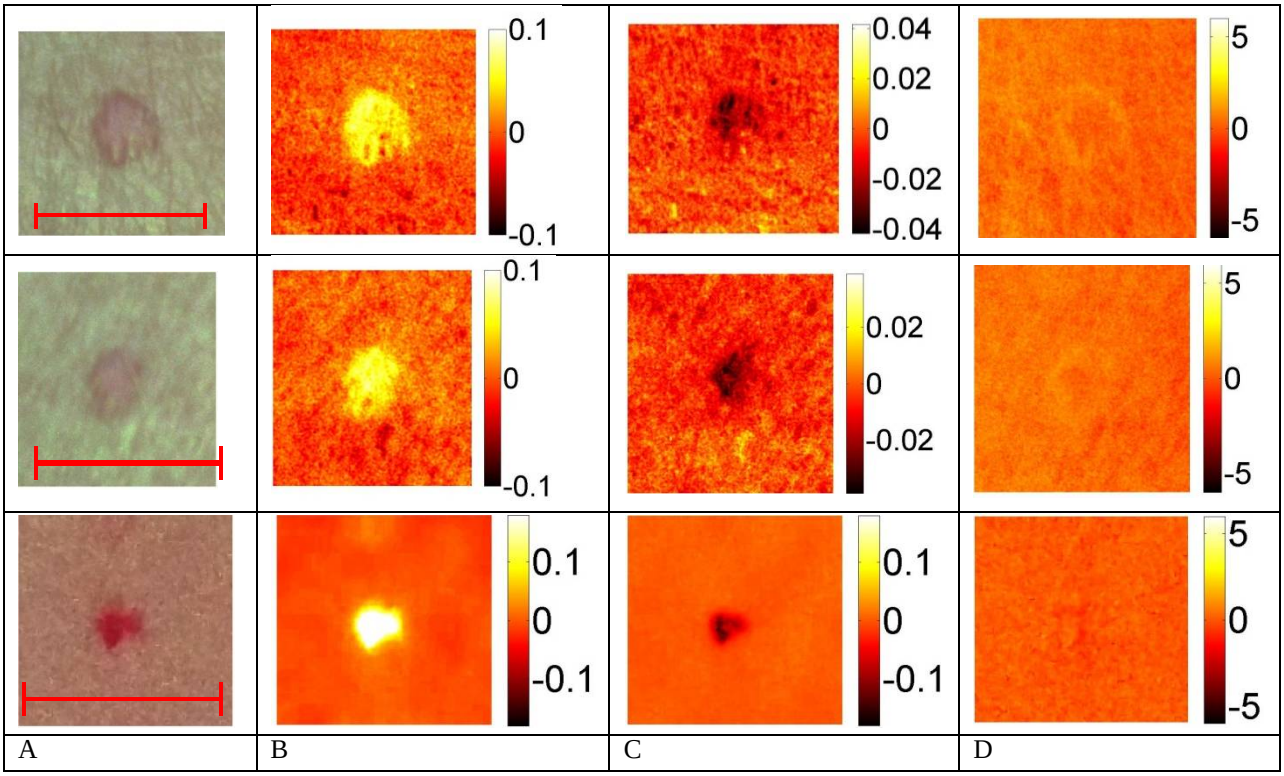

Fig.11. RGB image (A, scale bar 5 mm) and the corresponding maps representing chromophore concentration changes for three cases of vascular hemangioma: B – oxy-hemoglobin, C – deoxy-hemoglobin, D – melanin. Units of color scale – milimoles [mM].

After processing the clinical images, skin chromophore maps were constructed and changes of malformation's chromophore content with respect to the adjacent healthy skin could be evaluated. Clinical models assume that the pigmented skin lesions represent abnormal increase of epidermal melanin and the vascular lesions – increased supply of dermal arterial blood (rich of oxy-hemoglobin) to the superficial layers of skin. As initially expected, we observed notable melanin content increase in all cases of both pigmented malformations – nevi and seborrheic keratosis. Increase of oxy-hemoglobin content and decrease of deoxy-hemoglobin was observed in all examined vascular malformations – hemangiomas. For illustration, images for three typical clinical cases related to each of the examined three pathologies are presented on Figs. 9-11. The color photo of a malformation, taken under simultaneous three wavelength illumination (on the left – A), is compared with the obtained concentration distribution maps of oxy-hemoglobin (B), deoxy-hemoglobin (C) and melanin (D). All pathology data are related to the adjacent healthy skin ($\Delta c = 0$) so that only increased and decreased concentrations are quantified by colors.

Fig.9 shows how melanin content increases in nevi, without essential changes in the hemoglobin content. Similar responses were obtained from the other examined pigmented skin malformation - seborrheic keratosis (Fig.10). Quite different chromophore composition changes were recorded for vascular hemangiomas (Fig.11) – melanin concentration in the pathology remained practically unchanged while the oxy-hemoglobin content notably increased and the deoxy-hemoglobin content decreased in comparison to healthy skin.

The color scales in Figs.9-11 are calibrated in milimoles (mM), so the increased or decreased chromophore content can be quantitatively analyzed and/or compared. It might help dermatologists to characterize the severity of pathology if clinical thresholds for particular chromophores in the malformation are established.

Some clinical measurements were taken by means of the NEXUS5 smartphone and the new four-laser illumination device (Fig.4). As example, images of a bruise are presented in Fig.12. One can note that bilirubin concentration in a bruise is higher than in the surrounding skin, as expected. Besides, the obtained chromophore distributions of several common nevi, seborrheic keratosis and hemangiomas showed generally acceptable agreement with the related physiological expectations. However, the uneven illumination of skin created problems at the image processing stage, so re-design of the optical system appeared to be necessary for further studies.

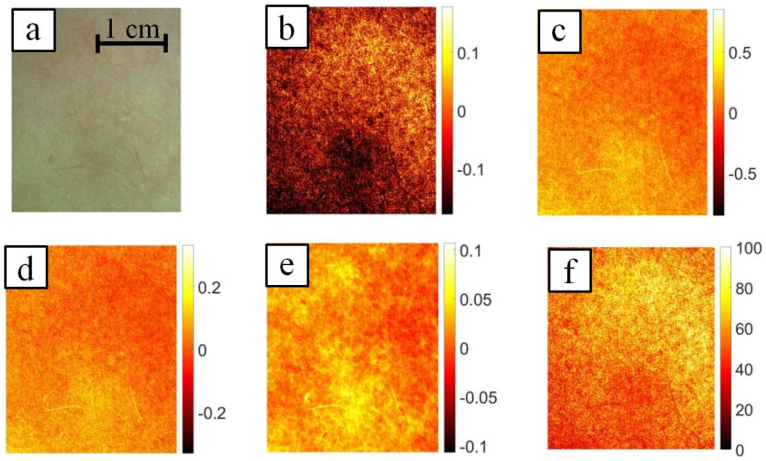

Fig.12. (a) RGB image of a bruise and the corresponding maps representing four chromophore concentration changes: (b) oxyhemoglobin, (c) deoxyhemoglobin, (d) bilirubin, (e) total hemoglobin, (f) oxygen saturation.

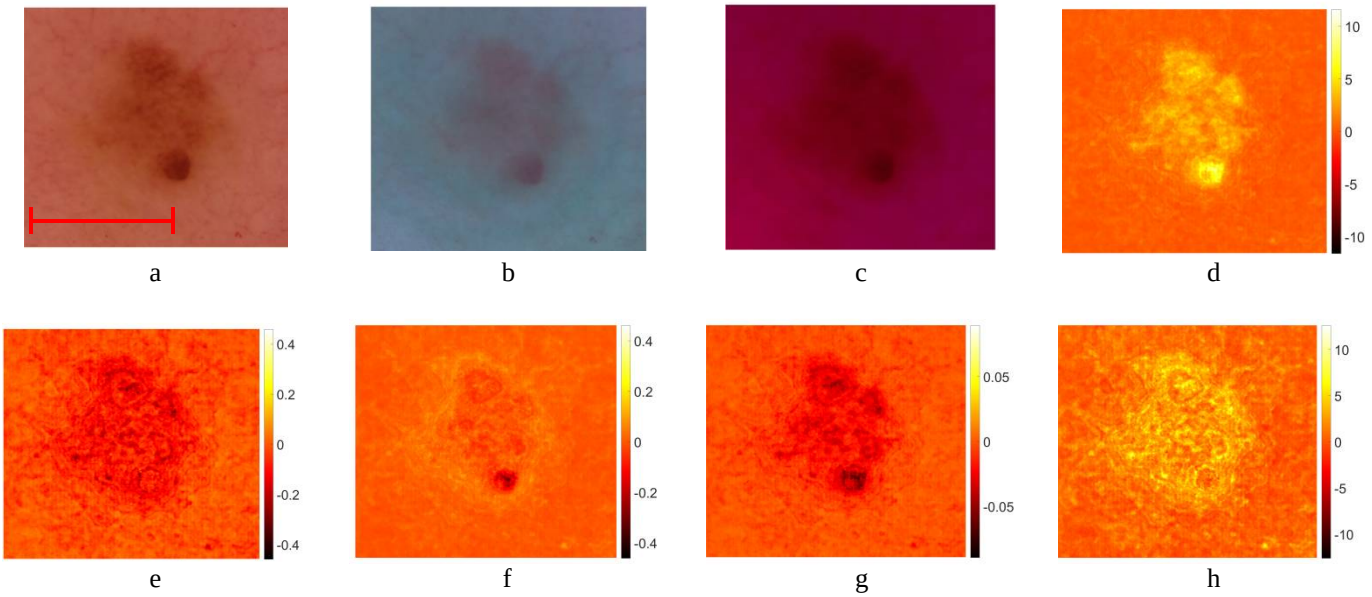

Fig.13. (a) RGB image of nevus (scale bar 5 mm). (b) RGB image when 450 nm, 525 nm and 849 nm lasers are turned on. (c) RGB image when 405 nm and 656 nm lasers are turned on. Corresponding maps representing chromophore concentration changes: (d) melanin, (e) oxyhemoglobin, (f) deoxyhemoglobin, (g) bilirubin, (h) lipids.

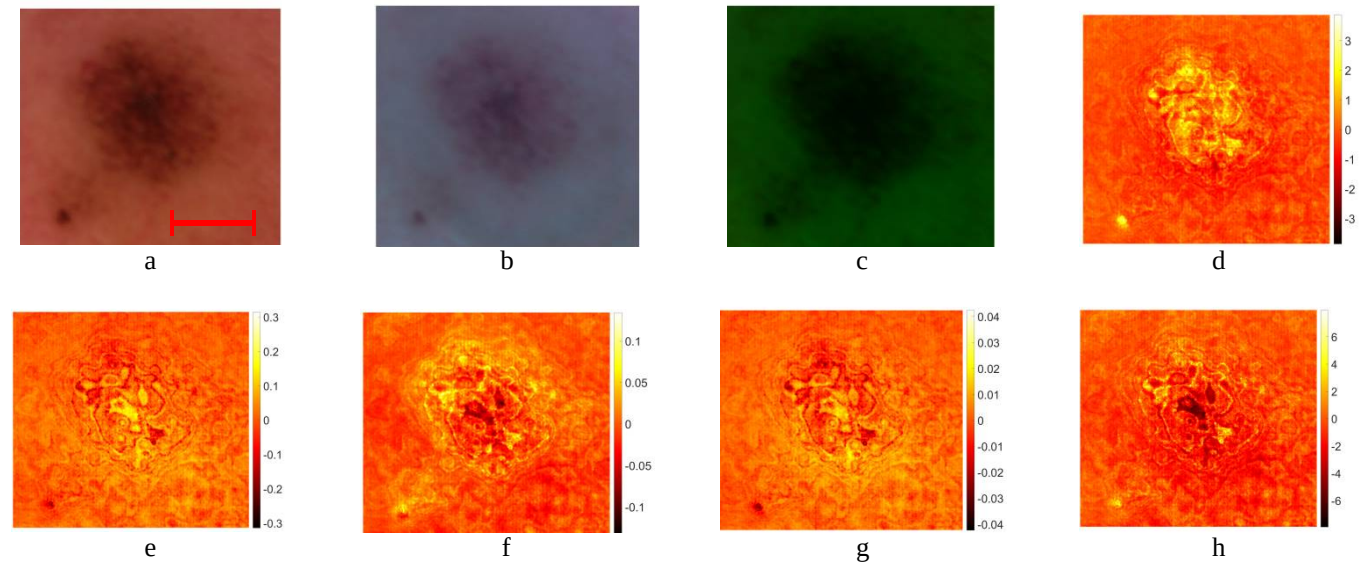

Fig.14. (a) RGB image of lentigo maligna (scale bar 5 mm). (b) RGB image when 405 nm and 656 nm lasers are turned on. (c) RGB image when 450 nm, 525 nm and 849 nm lasers are turned on. Corresponding maps representing chromophore concentration changes: (d) melanin, (e) oxyhemoglobin, (f) deoxyhemoglobin, (g) bilirubin, (h) lipids.

A systematic clinical study was performed using the newly developed 5-laser device, version 2 with improved illumination quality (Fig.8). Altogether 45 skin pathologies of 23 patients (7 male, 16 female, age range 25-71 years) with their written consent were examined - 5 hemangiomas, 1 lentigo maligna, 27 nevi and 12 seborrheic keratoses. The obtained chromophore maps (one example for each pathology) are presented in Fig. 14-18.

At the current stage it is difficult to comment these results. Accordingly to expectations, pigmented lesions show increased melanin content and vascular lesions – increased oxy-hemoglobin and decreased deoxy-hemoglobin level. Generally, figures 14-18 illustrate capability of the developed device to capture five high-quality single spectral line images. As this was our first attempt to calculate distribution maps of five skin chromophores, eventually some improvements in the processing algorithms (e.g. corrections due to different penetration depths and different intensities of the used illumination spectral lines) are to be introduced in further research.

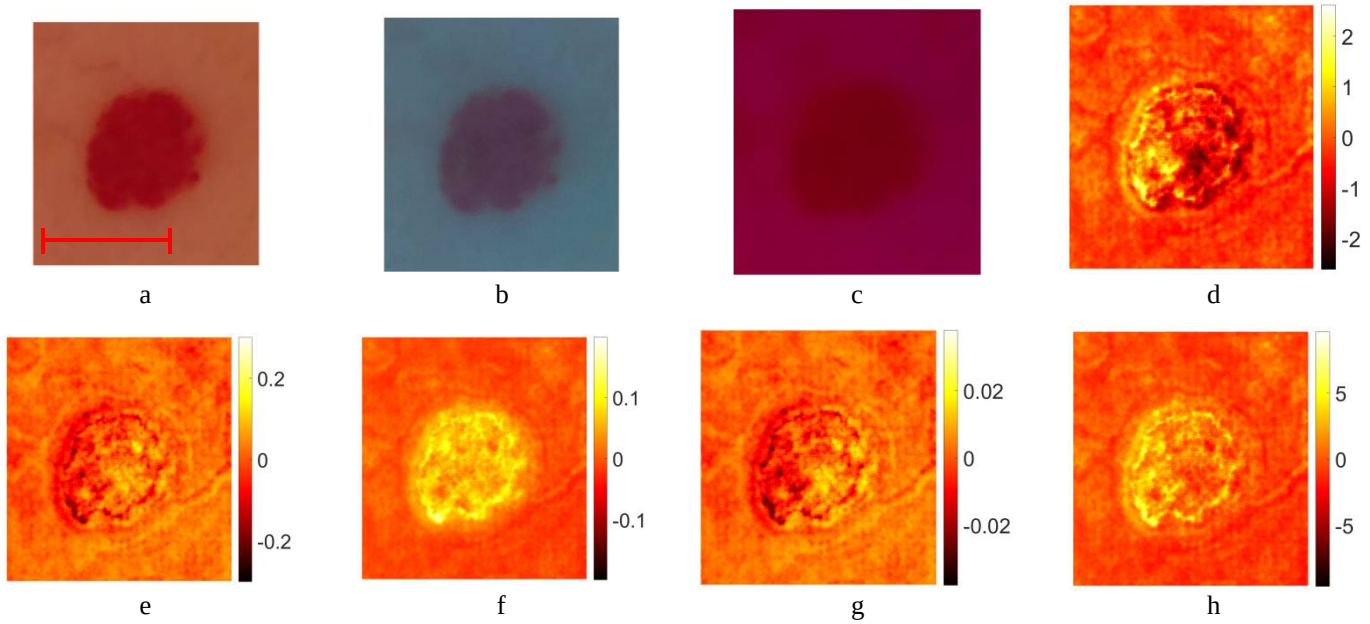

Fig.15. (a) RGB image of hemangioma (scale bar 5 mm). (b) RGB image when 450 nm, 525 nm and 849 nm lasers are turned on. (c) RGB image when 405 nm and 656 nm lasers are turned on. Corresponding maps representing chromophore concentration changes: (d) melanin, (e) oxyhemoglobin, (f) deoxyhemoglobin, (g) bilirubin, (h) lipids.

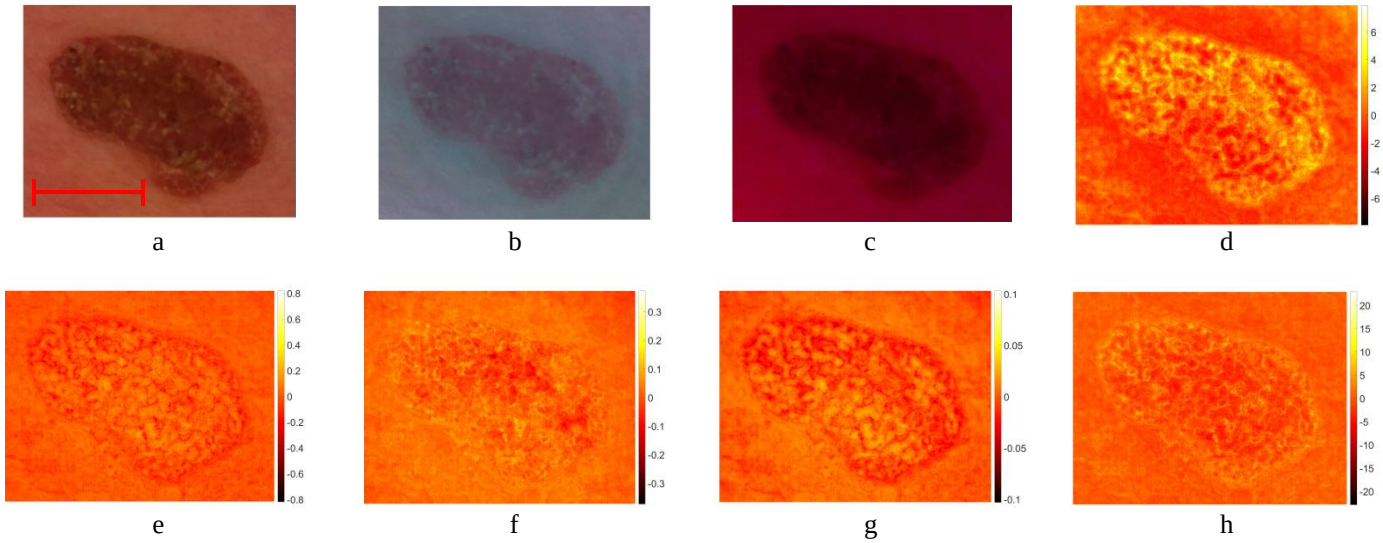

Fig.16. (a) RGB image of seborrheic keratosis (scale bar 5 mm). (b) RGB image when 450 nm, 525 nm and 849 nm lasers are turn on. (c) RGB image when 405 nm and 656 nm lasers are turn on. Corresponding maps representing chromophore concentration changes : (d) melanin, (e) oxyhemoglobin, (f) deoxyhemoglobin, (g) bilirubin, (h) lipids.

Counterfeit banknote detection by single-snapshot RGB imaging at triple wavelength laser illumination

NEXUS 5 smartphone-based prototype device with add-on light source emitting three discrete spectral lines at wavelengths 450nm, 532nm and 659nm was used also for comparative analysis of authentic and counterfeit 20 EUR and 500 EUR banknotes. The counterfeit banknotes have been taken out of circulation by the Bank of Latvia. Three monochromatic spectral line images at those wavelengths were extracted by a single snapshot as described above.

Comparison of single spectral line images of authentic and counterfeit banknotes of both nominal values revealed a number of differing features, especially at the 532nm wavelength. Fig.17 illustrates this for the same element of three 20 EUR banknotes – one authentic (a) and two counterfeit (b, c). The calculated spectral ratio images of the

same elements (e.g. 448nm/659nm image) provided even more distinguishable data for potential snapshot counterfeit detection by a smartphone (Fig.18).

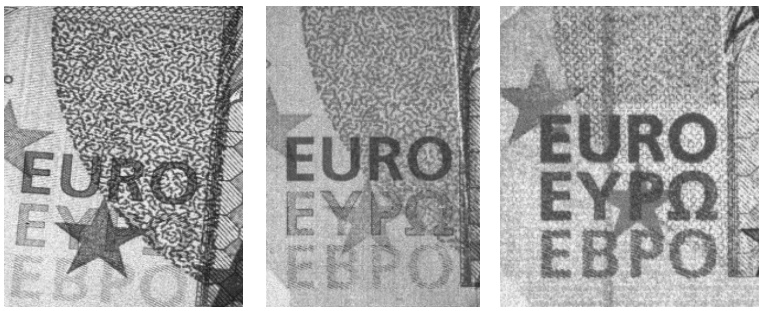

a b c

Fig. 17. 532nm spectral line images of the same fragment of 20 EUR banknotes: a – authentic; b, c – counterfeit.

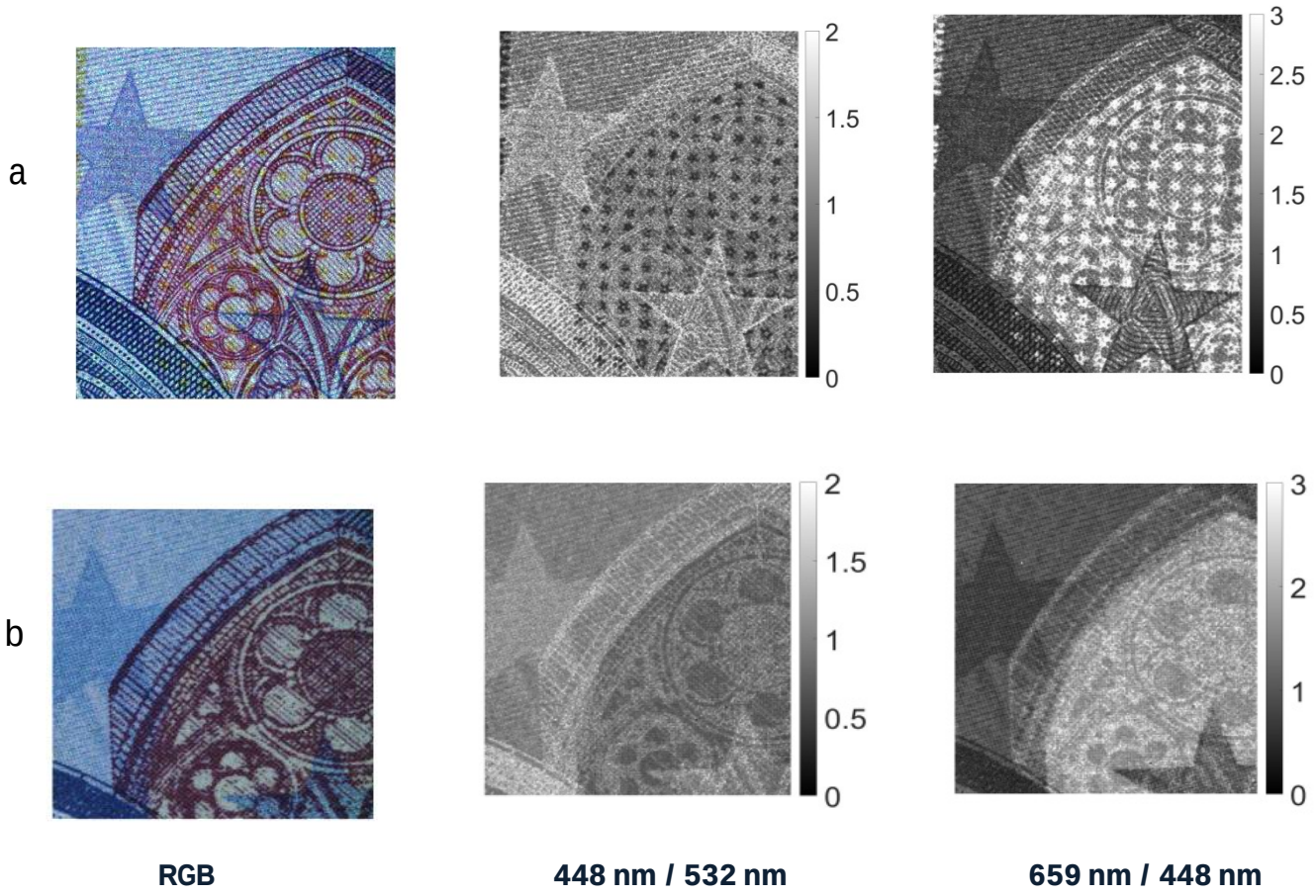

Fig.18. Comparison of color (RGB) and spectral ratio images of the same fragment of authentic (a) and counterfeit (b) 20 EUR banknotes.

Our first results confirmed the applicability of single spectral line imaging for smartphone snapshot detection of counterfeit banknotes. This approach might be used also in advanced money-counting machines. Counterfeits of other colored matters (e.g. documents, paintings) by this patented [9] method might be detected, as well. Further work includes development of methodology and software for routine applications of the proposed technique.

References of Chapter 1

1. J.Spigulis and L.Elste, "Method and device for imaging of spectral reflectance at several wavelength bands," WO 2013135311 A1 (2012).
2. J.Spigulis, D.Jakovels and L.Elste, "Towards single snapshot multispectral skin assessment," *Proc. SPIE* **8216**, 82160L (2012).
3. J.Spigulis and L.Elste, "Single snapshot RGB multispectral imaging at fixed wavelengths: proof of concept," *Proc.SPIE* **8937**, 89370L (2014).
4. S. Prahl, "Tabulated Molar Extinction Coefficient for Hemoglobin in Water," http://omlc.ogi.edu/spectra/hemoglobin/summary.html.
5. T. Sarna and H. M. Swartz, "The physical properties of melanin," http://omlc.ogi.edu/spectra/melanin/eumelanin.html.
6. J.Spigulis, M.Lacis, I.Kuzmina, A.Lihacovs, V.Upmalis, Z.Rupenheits. Method and device for smartphone mapping of tissue compounds. WO 2017/012675 A1, 2017.
7. J.Spigulis, I.Oshina. Method and device for chromophore mapping under illumination by several spectral lines. Patent LV 15106 B, published 20.03.2016.
8. U.Rubins, E.Kviesis-Kipge, J.Spigulis. Device for speckle-free imaging under laser illumination. PCT/EP2017/063565, 2017.
9. J.Spigulis, I.Oshina. Method for detection of colored counterfeits, LV patent application P-17-78, 2017.

2. Photoplethysmography video-imaging: prototypes, software and clinical results

The incident cw light can be reflected from the skin surface and also may enter its epidermal and dermal layers where light can be absorbed and/or scattered. A part of back-scattered photons have been travelled via the skin dermal layer where arterial blood volume periodically changes with each heartbeat. As a consequence, also total blood absorption changes with each heartbeat and the back-scattered light intensity is modulated - the detected so-called remission photoplethysmography (PPG) signal comprises a relatively stable DC component, determined by absorption of the "static" skin structures, and a pulsatile AC component caused by the periodically changing blood absorption. The pulsatile remission PPG signals can be detected not only by specially designed skin contact probes, but also distantly, e.g. by video-imaging of skin with subsequent signal processing. This technique is called PPG-imaging (PPGI) or remote PPG (rPPG). The captured video-signals consist of a number of image frames taken at a definite frame rate, e.g. 20 frames per second. Consequently, during one heart activity cycle (~1s) 20 skin images are obtained, each at different phase of the sub-cutaneous pulse wave. If consecutive frames are compared, the skin-remitted light intensity detected from a fixed area increases and decreases with time, forming the periodic PPGI signal. Specific software allows extracting the arterial pulsations from the video-signal over the whole imaged skin area. The amplitude of PPG peaks may differ between the image pixels due to different blood perfusion of the skin tissues - especially if there is a burn or other dermal skin damage. After the image processing, parametric maps of the PPG signal amplitude distribution (or blood perfusion maps) can be constructed.

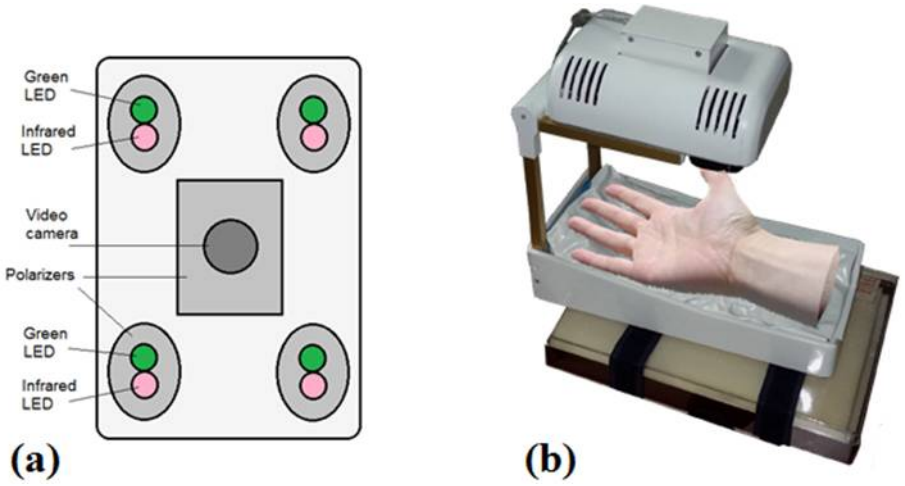

Fig.19 Dual wavelength photoplethysmography imaging device: bottom view of the imaging system - camera and light sources (a) and the whole device with vacuum pillow supporting the palm (b).

Fig.19 illustrates the recently designed PPGI prototype device for distant monitoring of anesthesia efficiency during the palm surgeries. The system was intended for recording signals from the curved surface of the hand (dorsal or ventral aspect). The illuminator comprised four bispectral light sources, each consisting of two high-power LED emitters (*Roithner LaserTechnik GmbH,* green: λ=530nm, 3W and infrared: λ=810nm, 1W). To achieve uniform illumination of skin surface, adjustable LED intensity control was introduced via PC based custom developed software. The two wavelengths of illumination were chosen in order to control blood pulsations at two different vascular depths in real time. The microcontroller board (Arduino Nano, Arduino, USA) provided sequential switching of green and IR LEDs and triggering of the captured video frames. The camera control was performed by *uEye* software using manual trigger mode, fixed exposure time, 2x2 pixel binning and triggered at 60 frames/s. The monochromatic camera (8 bit CMOS *IDS-uEye UI-1221LE*) was equipped with *S-mount* 1/2 inch F=4mm low distortion, wide-field lens (Lensagon). The camera lens was placed at 15cm distance from the skin surface so ensuring full view of adult palm (20x15cm field of view). In order to reduce skin specular reflectance, orthogonally oriented polarizers were placed behind the camera and all four light sources, respectively. The plastic parts were

produced by a 3D printer (*Prusa i3*, custom made, Latvia). The device comprised a plastic enclosure filled with an adjustable vacuum pillow (40x20 *AB Germa*, Sweden) as the palm support.

Another, much smaller PPGI prototype device (Fig.20) for more universal applications related to skin microcirculation control has been developed, as well. It involves near-infrared LED illuminator and a video camera, both placed in custom designed 3D-printed case (4×4×4 cm). The illuminator comprises a ring of twelve circularly oriented near-infrared LEDs (peak wavelength 760nm, current 20mA each), connected in parallel; stabilized illumination is provided by LED driver (cat4104). Video acquisition is performed by a board-level CMOS video camera (*IDS uEye UI-1221LE*), resolution 752×480pix, maximum framerate 87fps., 8-bit monochrome).

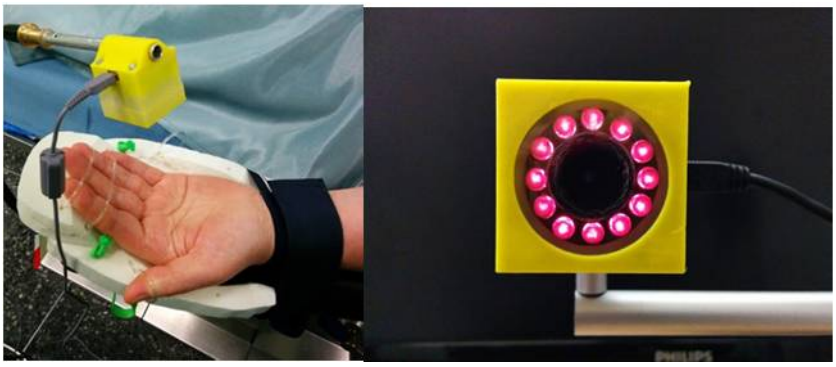

Fig. 20. The compact PPGI prototype device in operation (left) and the front view of the device (right).

The camera is equipped with low-distortion S-mount 4mm lens (*Lensagon*). In order to reduce skin specular reflectance, cross-oriented polarizers are placed behind the light sources and in front of the camera, respectively. The infrared cut-off filter KC-15 (>700nm) also is placed in the front of the camera, in order to minimize the influence of ambient illumination. USB-2 cable connection to PC ensures both video-signal processing and the power supply.

For real clinical applications, it is a good choice to use surgical lamp as a light source. A simple and convenient PPGI system for contactless monitoring of anesthesia effectiveness before and during surgical procedures has been developed (Fig.21). The system involves compact lightweight camera (Ximea-xiQ, CMOSIS, ADC-8/10/12-bits, resolution 640x480, 502 frames/s) with a low-distortion lens (Edmund Optics 3.5mm f/2.4) and green band-pass filter (half-bandwidth 520-580nm). Both are placed in a custom designed 3D-printed case, adapted for handle attachment to the warm-white-light surgical lamp (ALM Prismalix PRX800), see Figure 21,b. The camera is connected via USB-3 cable to a laptop computer which also serves as the power supply of camera. Video acquisition frame rate is 100 Hz (equal to the lamp blinking frequency), so temporal variations of the lamp intensity do not affect the PPGI signal, filtered in the frequency range 0.7-3.0 Hz.

a **b**

Fig. 21. The PPGI device attached to a surgical lamp (a) and the design of its holder (b).

Software solutions for PPGI measurements

The proposed approach combines spatial and temporal processing to emphasize subtle temporal changes in a video. The process is illustrated in Fig.22. First, video images are received from the video camera and stored as an image cube of size H×W×B (H-height, W-width, B-buffer length). Then image cube is decomposed into a number of different spatial frequency bands. These bands have different signal/noise ratios due to different resolutions. The goal of spatial processing is in a simple way to increase signal-to-noise ratio by pooling multiple pixels; processing of down-sampled images is also less expensive. For this reason, we compute a full Gaussian pyramid, the size of dataset then is H×W×B + H/2×W/2×B+…+H/L×W/L×B, where L is the height of pyramid.

The next step is temporal processing of image dataset. The value of each pixel changes from frame to frame and reflects a subcutaneous blood volume changes. Fast varying rPPG (AC) component is related to cardiac activity. The AC signal is extracted by applying a bandpass filter within the heartbeat frequency range. We suppose heartbeat interval 40-100 bps for most of the subjects, so the frequency range 0.7-2 Hz is chosen. The temporal processing is uniform for all spatial levels and for all pixels within each level. Further, the amplitude maps are calculated in all spatial levels within a frame buffer, and the final size of dataset is H×W +…+ H/L×W/L.

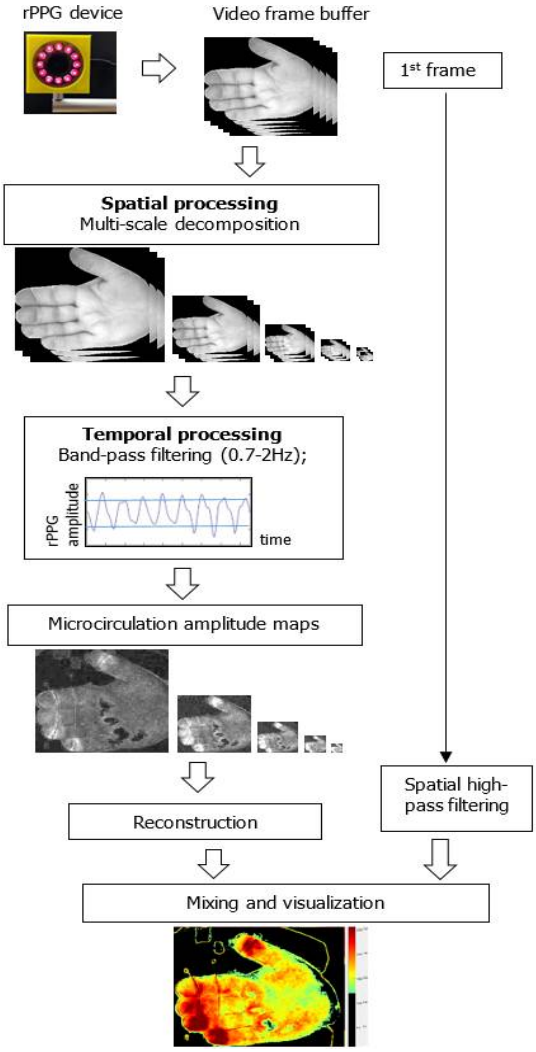

Fig. 22. The block-diagram of rPPG imaging algorithm.

Next step is reconstruction of resulting amplitude map from multiple images. This is done by collapsing the spatial pyramid to obtain the final output of size H×W. Each pyramid image is multiplied by a coefficient, which leads to amplification of the consequent spatial component.

The final step is visualization of the processed rPPG map. This includes normalization, thresholding and color-indexing of resulting map. The first frame of video is spatially high-pass-filtered and overlaid to map in order to

maintain grain details in the resulting map. All algorithmic steps described above could be repeated infinite times. The only limiting factor of the acquisition time is computer memory.

Every step of processing will be described below in more details, using mathematical equations.

The spatial decomposition

Spatial decomposition was done by Gaussian pyramid calculations. Here subsequent images are weighted down using a Gaussian average (Gaussian blur) and scaled down. Each pixel contains a local average that corresponds to a pixel neighborhood on a lower level of the pyramid. The base level is defined as the original image *I*(*x*,*y*). The Gaussian pyramid is defined recursively as follows:

$G_1(x, y) = I(x, y)$, for level: $l = 1$

$$G_l(x, y) = \sum_{m=-2}^{2} \sum_{n=-2}^{2} w(m, n) \cdot G_{l-1}(2x + m, 2y + n), \quad (3)$$

otherwise: $l = 2,3 \ldots L$

where *L* is the number of pyramid levels, *w*(*m*,*n*)=[1 4 6 4 1]/16 is a weighting function or kernel, which is similar for all levels of the pyramid. The pyramid is calculated for each video frame.

The temporal filtering

Temporal processing of image dataset is performed by calculating the corresponding pixel value changes in predefined frequency range. To extract fast-varying AC component, infinite response (IIR) filter was used. The IIR filter can be successfully used for real-time signal filtering thanks to its simplicity and computational inexpensiveness. The 2nd order Butterworth band-pass filter in the frequency range 0.7-2 Hz was applied for calculating the pulsatile heartbeat component. The output pixel value Sn then can be found recursively from last 5 video frames:

$$\begin{aligned} S_n = {} & 0.006 \cdot G_n - 0.012 \cdot G_{n-2} \\ & + 0.006 \cdot G_{n-4} \\ & + 3.7278 \cdot S_{n-1} \\ & - 5.2542 \cdot S_{n-2} \\ & + 3.3194 \cdot S_{n-3} \\ & - 0.7935 \cdot S_{n-4} \end{aligned} \quad (4$$

Temporal filtering is applied to all pixels of video, for all pyramid levels.

The amplitude map

The mean amplitude of rPPG AC signal is calculated for each pixel of images, within a frame buffer. For increased computing speed, the calculation of total sum of all numbers is performed in the following way: first is calculated total sum of all the numbers *A*, then subtracted the last element and added first element of sum buffer. The recursive formula is defined as follows:

$$A_n(x, y) = \frac{1}{N} \sum_{n=0}^{N} |S_n(x, y)|, \quad \text{if } n \leq N \quad (5$$

$A_n(x, y) = A_{n-1}(x, y) + |S_n(x, y)|/N - |S_{n-N}(x, y)|/N$,

n > N

where A is the sum of AC signal within buffer, N is a buffer length.

The reconstruction

The reconstruction of resulting image is done by collapsing the spatial pyramid to obtain the final output. Each pyramid image is multiplied by a coefficient, which leads to amplification of the consequent spatial component. The final image is found by recursive formula:

$$A_{l-1}(x,y) = A_{l-1}(x,y) + c_{l-1} \cdot A_l(\|x/2\|, \|y/2\|) \qquad (6)$$

$$l = L, L-1, L-2, \ldots 2$$

$$R(x,y) = A_1(x,y)$$

where $R(x,y)$ is reconstructed image, the coefficients cl determines the attenuation of different spatial components. We found empirical relationship between the coefficients c_l and pyramid level l, which is defined by power of attenuation p:

$$c_l = p^{l-1}, \qquad l = 1,2 \ldots L-1 \qquad (7$$

Finally, the amplitude map is calculated by subtracting "zero" level from the reconstructed image. Physiological "zero" level is detected, when the microcirculation signal is masked by noise in cases when the pulse signal is too low for detecting rPPG signal.

The software has implemented algorithms described above and it was adapted for computers having touchscreen displays. It was tested with the developed rPPG device, using Lenovo Yoga-2 portable computer (I-5, 2.5 GHz, 8GB RAM, Windows-10 OS).

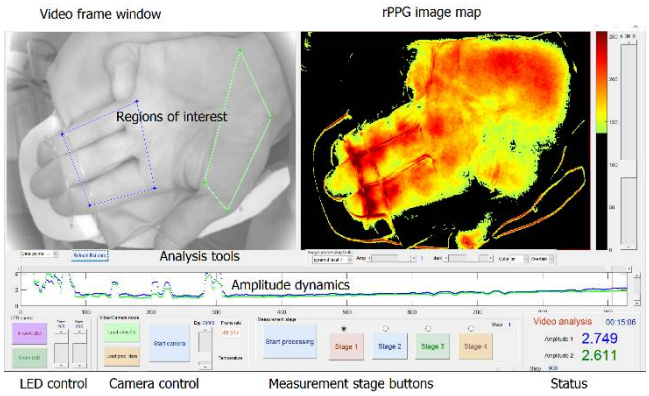

Fig. 23. The graphical user interface of rPPG imaging software.

The graphical user interface (GUI) of rPPG software is shown in Fig.23. It has several parts: 1) two large windows displaying a current video frame and rPPG image map; 2) signal window (in center) displaying mean-averaged rPPG amplitude signals from two manually selected regions of interests (RoI); 3) LED control panel (for controlling of LED intensity of device, described in [11]); 4) video camera control panel (start/stop preview, exposure control, frame rate control and camera sensor temperature); 5) measurement stage window, including Start/Stop analysis button and buttons for setting time markers of predefined measurement stages; 6) status window displaying current procedure, clock time, timer and RoI-averaged rPPG amplitudes; 7) image processing tools (colormaps, map threshold level, pyramid level and power of attenuation).

The software is operating in two modes: 1) real-time acquisition/analysis and 2) analysis of recorded data. During the acquisition, the software records video sequence (avi mpeg-4 stream) and processed data sets (rPPG image pyramids, RoI positions, markers, etc. – in Matlab mat file).

Gaussian pyramid tests

We tested how the number of Gaussian pyramid levels affects the quality of rPPG maps. The goal of study was to understand which is the optimal number of pyramid level L. Higher L value leads to increased amplification of low

spatial components, so the microcirculation signal rises above the camera sensor and quantization noise. On the other hand, higher *L* leads to over-blurring of image, so the details of microcirculation map become hidden.

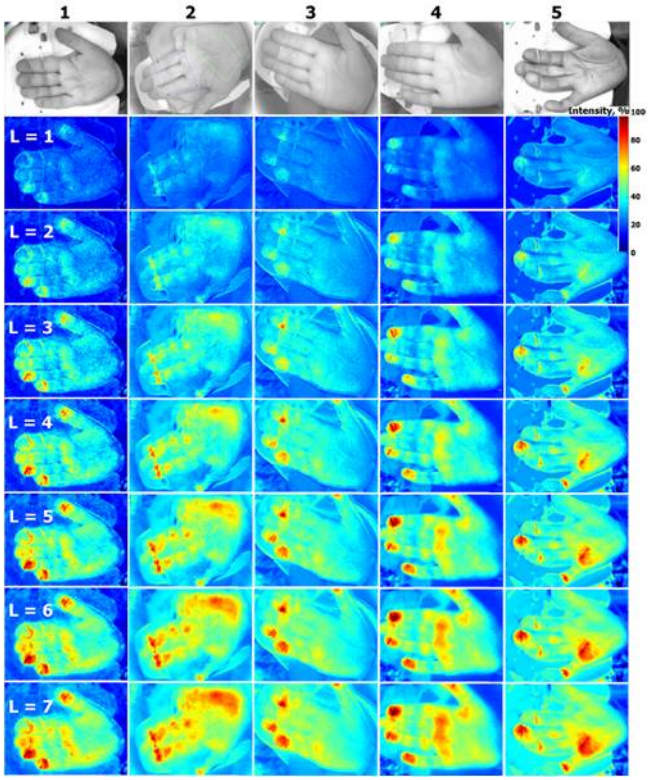

Fig. 24. The rPPG amplitude maps taken from 5 patients after the local anesthetic input. Image maps calculated at different pyramid levels *L*.

Fig.24 shows the test results of five measurements. The rPPG amplitude maps show high details starting from *L*=3, but optimal amplitude-detalization is appreciated as *L*=5. Study showed that larger L values did not improve the quality of maps.

Comparison of RPPG maps with thermal images during the RA procedure

Monitoring of skin perfusion during the regional anesthesia is important as an appraisal for potential clinical application of the rPPG system. Local anesthetic affects the sympathetic vascular tone by resulting vasodilation and

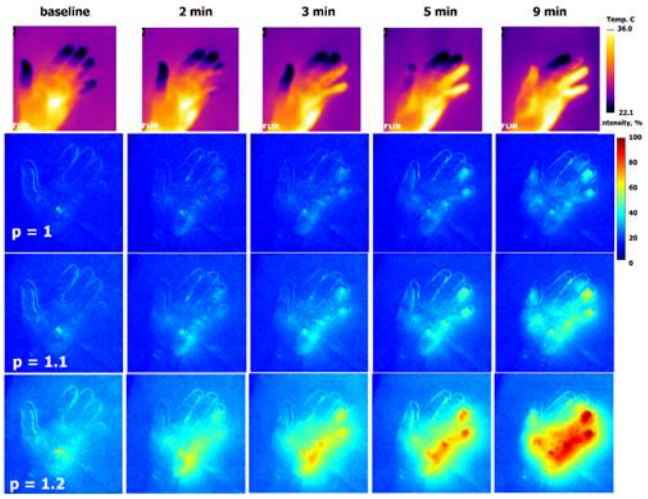

Fig. 25. The thermal images (above) and rPPG amplitude maps taken before (baseline) and after RA procedure (2 min, 3 min, 5 min and 9 min later). Calculations were done by different attenuation parameter *p* values.

subsequent rising of microcirculation intensity. Skin microcirculation changes can be detected by our system during RA. To confirm the applicability of our technique, the obtained rPPG images were compared with the thermal images

of skin. Thermal imaging is a verified method for monitoring of skin microcirculation changes caused by local anesthetics, therefore we used thermography as the reference method.

The maps were calculated at 5 measurement stages: the baseline (before the RA procedure) and at four time moments after the injection of local anesthetics. Fig.25 shows thermal images of palm and rPPG image maps at

different attenuation values p. Results confirmed that higher p value increase the sensitivity of RA detection, but too high p value leads to over-blurred map image. Gradual increase of skin perfusion was observed three to nine minutes after administration of the local anesthetics.

Skin blood perfusion measurements with the PPGI prototypes

In order to evaluate ability of the double-wavelength PPGI prototype (Fig.19) to discriminate between cutaneous superficial and deep plexus perfusion, hyperemia of superficial plexus was induced by vasodilatory liniment (Transvasin, Seton, UK). PPGI signal amplitudes at both spectral bands of illumination (peak wavelengths 530 nm and 810 nm) were recorded; Laser Doppler imaging (LDI) signals were captured in parallel by a certified commercial device. Ten healthy volunteers (5 males and 5 females, skin type II) were recruited to participate.

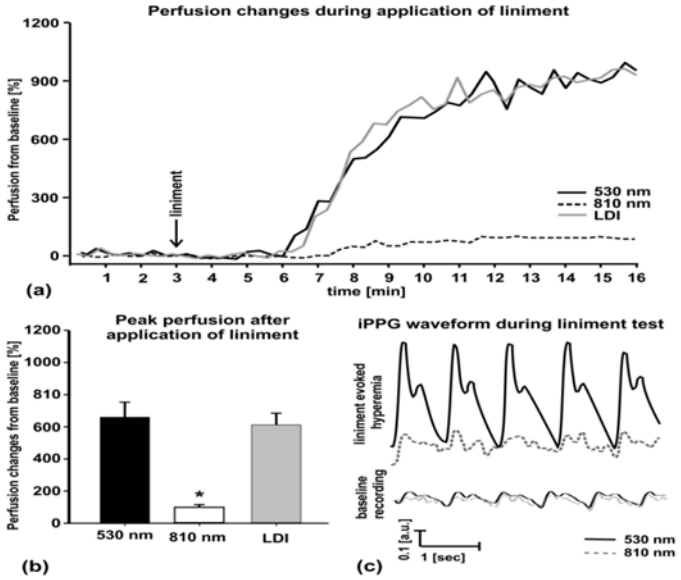

Fig.26. Liniment-induced skin perfusion changes as registered with the double-wavelength PPGI prototype and commercial LDI device (a), peak perfusion increase from the baseline (b) and the PPGI signal waveforms before and after provocation (c).

The subject was seated on a comfortable reclined chair with the right hand at the dorsal aspect, fixed on the vacuum pillow support and kept at heart level, with fingers tightly fitted to avoid movements. The protocol involved 3-minute recording of the baseline followed by topical application of liniment and signal recording for 12 minutes. Within three to four minutes after application of liniment the reddening of skin appeared, indicating to hyperemia. Green PPGI measurements showed essential (about 6 times) increase of superficial skin perfusion, well correlated to that measured by the LDI device, while the NIR PPGI signal amplitude (reflecting arterial blood perfusion in deeper dermal layers) only slightly increased – see Fig.26. This result convincingly demonstrates the functional abilities of the developed double-wavelength prototype for non-contact skin microcirculation monitoring.

Local anesthesia affects the sympathetic vascular tone, resulting in vasodilation and raised skin blood perfusion. This increases the amplitude of fast-varying signal detected by the PPGI prototypes – see Fig.27 for illustration. Such physiological response makes possible to detect remotely, if and when anesthesia works just by following the changes in amplitude of the detected PPG signals.

Fig.28 presents the PPG signal amplitude dynamics in response to regional anesthesia of patient's palm before surgery, as detected by the PPGI prototype attached to the surgical lamp (Fig.21).

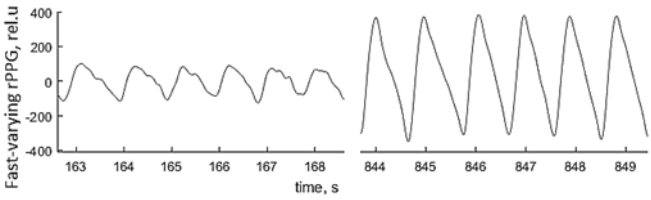

Fig. 27. The palm PPGI signal waveforms before (left) and after (right) administration of local anesthetic.

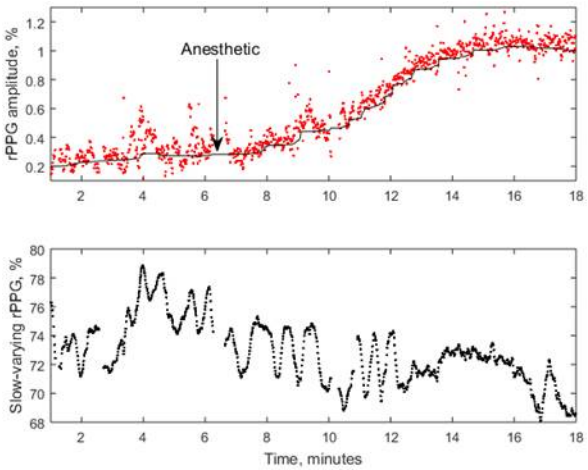

Fig. 28. The averaged amplitude of fast-varying PPG signal (above) and slow-varying signal (below) during the regional anesthesia procedure.

The graph above shows the beat-to-beat amplitude dynamics while the graph below represents temporal variation

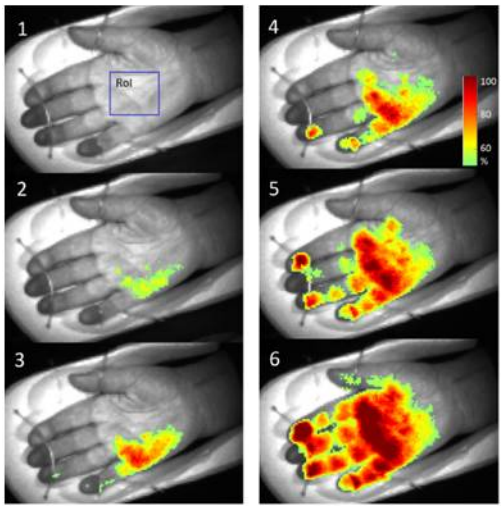

Fig. 29. PPGA maps before (1) and after the administration of local anesthetic: 2 – 1 minute, 3 – 3 minutes, 4 – 5 minutes, 5 – 6

minutes, 6 - 7 minutes later. of the slow-varying PPGI component. Gradual increase of perfusion with subsequent rise of the PPGI signal amplitude (the upper graph) was observed few minutes after the administration of local anesthetics. The plateau phase - stable increased skin perfusion induced by the anesthetic - was reached approximately 10 minutes later and indicated the possible surgery starting time.

Fig.29 shows several screenshots of palm video fused with PPG-amplitude (PPGA) maps during anesthetic action before the surgery. As the local anesthetic affected four different nerves, subsequent microcirculation changes at four different palm skin zones (dermatomes) were observed. The PPGA maps showed increased microcirculation in dermatomes immediately after the local anesthetic was administered (stages 2-6).

To conclude, the obtained results clearly confirm clinical efficiency of the developed PPGI prototypes for remote patient anesthesia monitoring before and during surgeries.

3. Laboratory and clinical measurements of human skin properties in the near-infrared range

Studies of human skin in the near infrared spectral range of 900–1700 nm have been performed in order to evaluate the potential of optical methods for assessment (and, eventually, visualization) of skin hydration and lipid content. Absorption of water and lipids in the NIR range is much higher than in the visible range; their absorption spectra partially overlap, as illustrated in Fig.30 for the spectral range 900-1300nm.

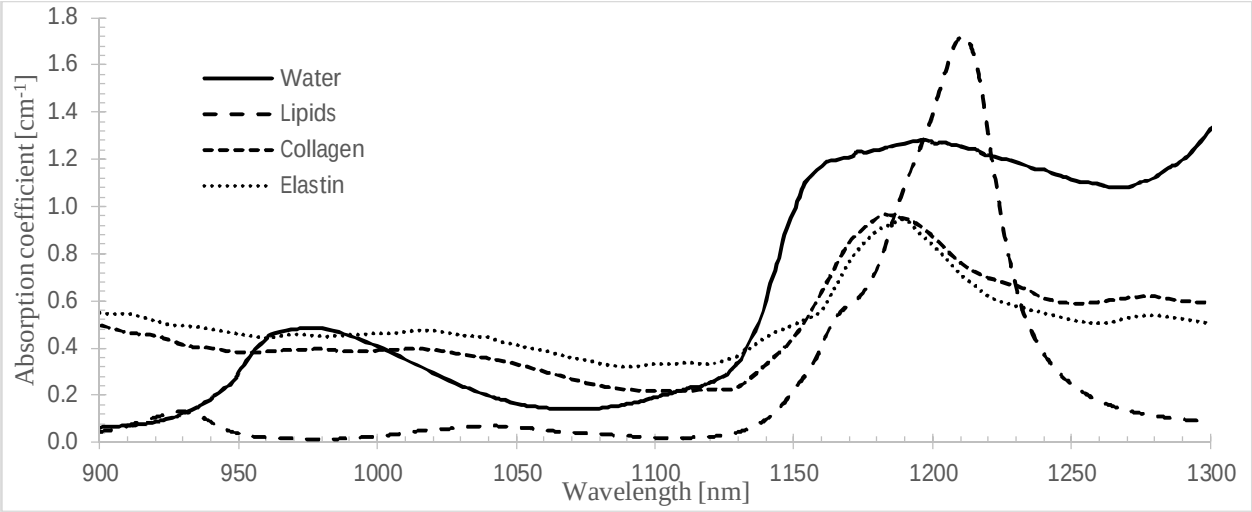

Fig. 30. Skin chromophore absorption spectra in the 900-1300 nm range.

Experimental setup consisted of a near-infrared spectrometer (*NirQuest 512* by *Ocean Optics*) in the spectral range of 900–1700nm, Y-type water free (WF) optical fiber probe, a stabilized tungsten-halogen light source (*SLS201/M* by *Thorlabs*) with radiation spectrum between 300 and 2600 nm, and a 3D printed nozzle as a spacer to separate skin from the detection and illumination fibers (Fig. 31). Optical fiber probe consisted of 6 illumination fibers (each 400 in diameter) in a circle around 1 detection fiber (400 in diameter) without any separation. The distance between optical fiber ends to the skin surface of interest was kept constant of 5 mm by the nozzle (outer diameter 25 mm, inner diameter 4 mm).

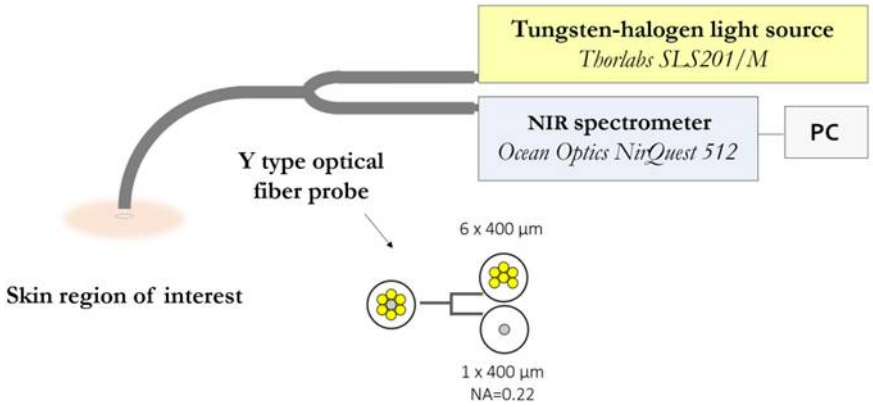

Fig. 31. Experimental setup for near-infrared diffuse reflectance measurements of skin.

During the measurement (up to 5 minutes), the nozzle was kept fixed on the skin surface by using a tripod. The arm of a volunteer was kept as motionless as possible during the whole measurement as diffuse reflectance spectrum is very sensitive to even the slightest of movements. The room temperature was approximately constant throughout all the measurements ( ). Temperature of the arm was measured before each measurement.

A similar setup was used to test how the distance between illumination and detection fibers affects the diffuse reflectance spectrum. This experimental setup consisted of two separate fibers (each fiber 600 μm in diameter) and a different 3D printed nozzle was used which consisted of 10 small holes next to each other to separate the centers of two fiber probe ends by 1.9, 3.8, 5.7, ..., 11.4 mm, 1.9 mm being the distance between centers when the fiber ends are exactly next to each other.

The setup of two separate fibers was used to test how the distance between fibers affects the diffusely reflected spectrum. Fig. 32 shows the absorption spectra depending on the distance between illumination and detection fibers. Only fiber separation up to 11.4 mm with sufficient S/N ratio is shown and wavelength range up to 1300 nm as around the 1450 nm water absorption maximum the results were too noisy. Fig. 33 shows the difference between absorbance values at the local absorption maximum (1200 nm) and the minimum (1050 nm). We can observe that by increasing the illumination and detection fiber difference, the difference in absorbance between local minimum and maximum increases linearly.

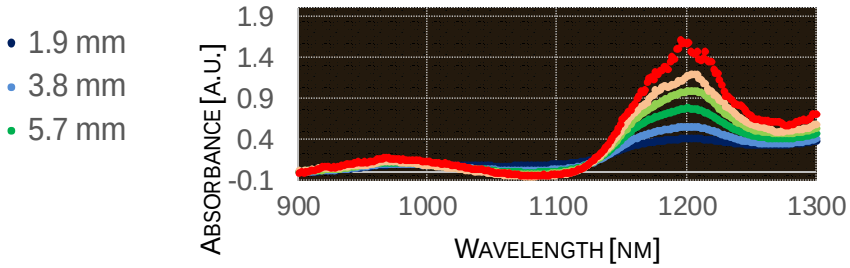

Fig. 32. The mesured absorption spectra of skin at different distances between illumination and detection fibers.

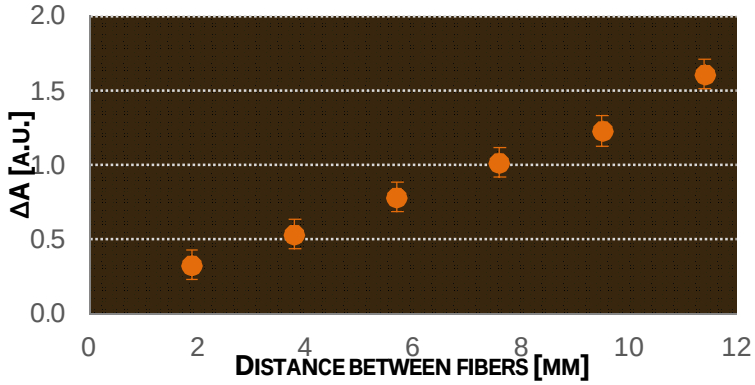

Fig. 33. Difference between the absorbance values at local absorption maximum (1200 nm) and minimum (1050 nm).

Clinical measurements

Experimental setup (Fig.31) comprised optical fiber probe consisting of 6 illumination fibers (each 400 μm in diameter) in a circle around 1 detection fiber (400 μm in diameter) without any separation. Due to very small separation between detection and illumination fibers (0,4 mm between the fiber centers), we expected to detect diffuse reflected signal from mainly the superficial layers of skin (the upper sublayers of epidermis).

We measured reflected intensity from skin surface I in the whole 900-1700 nm range by using the near-infrared spectrometer. We used a white reference tile *Avantes WS-2* that reflects 98% of the radiation in the spectral range 350-1800 nm to measure illumination spectrum I_0; in this measurement, the fiber probe end was kept at a 5 mm distance from the reference tile. We then converted reflected intensity values to optical density (OD) values based

on Beer-Lambert-Bouguer law. OD values represent absorption in tissue due to mainly water and lipids in this spectral range. Correction for dark current ( ) was also applied:

$$OD(\lambda) = \log_{10} \frac{I_0(\lambda) - I_{dark}(\lambda)}{I_0(\lambda) - I_{dark}(\lambda)} \qquad (8)$$

A typical OD spectrum of skin in the spectral range of 900-1700 nm is shown in Fig. 34. There are three main absorption maxima: at around 980 nm, 1200 nm and 1450 nm. The first two (980 nm and 1200 nm) are from a vibrational overtone of the O-H bond, while the maximum at around 1450 nm is due to the first overtone of the O-H stretching.

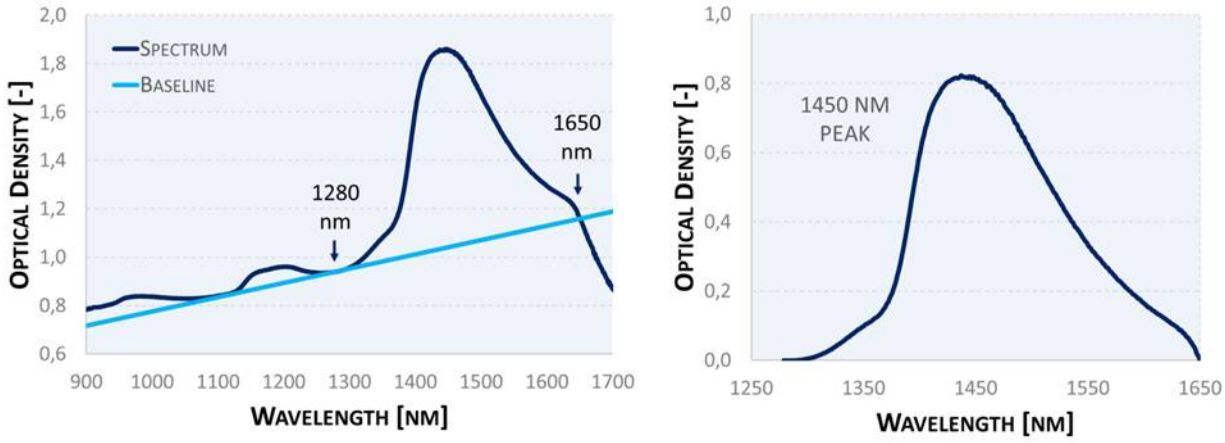

Fig. 34. Left: Example of an Optical Density (OD) spectrum of *in vivo* forearm skin and a baseline; Right: Baseline-corrected 1450 nm absorption maximum

For estimation of skin hydration, we chose the water absorption maximum at 1450 nm as it has the highest water absorption in this range, thus it is more sensitive to small changes in water volume fraction, compared to the other maxima. Due to high absorption around the water absorption maximum at 1450 nm, radiation around these wavelengths should not penetrate as deep in the tissue as other wavelengths in this spectral range, and in this study, we were mainly interested in the very upper sublayers of epidermis. We estimate that the radiation penetration depth around the water absorption maximum at 1450 nm is approximately 1 mm. However, the measurement depth should be lower due to very small illumination and detection fiber separation. Measurement depth of *DermaLab*, however, is much smaller – around 15 µm.

To eliminate scattering effect on OD spectrum, we used linear baseline correction between local minima at 1280 nm and 1650 nm (Fig. 34). After baseline correction, we calculated the volume area under the 1450 nm maximum which we chose as a parameter representing skin hydration.

We performed a clinical study to compare our developed system based on NIR spectroscopy and a commercial device *DermaLab*. In this clinical study, we tested the short-term (30 minutes) and long-term (1 month) effect of a moisturizing cream (developed by MADARA Cosmetics, Riga, Latvia) on skin hydration. In total, 39 volunteers (females, age range 18 – 60, average: 45, standard deviation: 12) participated in this study. The study protocol was approved by the local ethics committee, and each participant gave a written informed consent before the trial. A primary screening procedure was done by a dermatologist before the study. Measurements were performed in January and February in Riga, Latvia with outside temperature around 15 C (January) and around 0 C (February). During the measurements, room temperature was kept constant at around 23 C, and all participants were asked to sit at rest for 15 minutes at room temperature before the start of the measurements. All measurements were performed by two different devices - the developed device for estimation of skin moisture level by near-infrared

spectroscopy, and a commercial device *DermaLab* which estimates skin hydration based on changes in skin conductance (with an increased water volume fraction in skin, there is an increase in electrical conductance of skin).

In the beginning, after the participant had sat still for at least 15 minutes, one measurement on right forearm (control) and three measurements on left forearm (Fig. 35) were performed by both devices. For the short-term (30 minutes) study, dermatologist applied the moisturizing cream on the proximal part of volar aspect of left arm. Afterwards, the participant was asked to wait for 30 minutes in a room at a temperature of 23 °C, and another set of measurements were performed 30 minutes later - one measurement on right arm (control) and three measurements on left arm (where the cream had been applied). Three measurement points for left forearm were chosen due to possibly uneven application of the cream throughout the area. An average of the three measurements of left arm was later calculated and used for further analysis.

For the long-term study (1 month), participants were using the same moisturizing cream once a day on the same area of left forearm every day for one month. On the contrary, they were asked not to use any cream on the volar aspect of the right arm for the whole month. After 1 month, they came for another visit. After they had sat down still for at least 15 minutes to adapt to the room temperature, the same set of measurements was performed as in the beginning - one measurement on right arm (control) and three measurements on left arm where they had been applying the cream for the whole month.

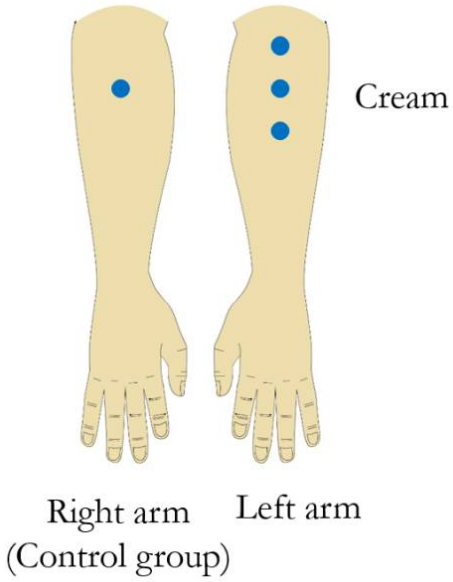

Fig. 35. Measurement points on the proximal part of volar aspect of the right forearm (control group) and left forearm (cream group)

In results, separately for both devices, we calculated the increase (in percent) in skin hydration parameter 30 minutes/1 month later compared to the beginning of the study as the average for all 39 participants (ΔV), as well as the standard error (SE). At first, we performed Lilliefors test in *Matlab* to test whether each measurement group (e.g. data of control group in the beginning of the study of all 39 participants) corresponds to normal distribution. Afterwards, a Two-Sample T-Test was performed on two respective groups (e.g. control group in the beginning and control group 30 minutes later) to test whether there is a statistically significant difference between both groups, in other words, whether there is a statistically significant difference between results 30 minutes (or 1 month) later for all participants, compared to the beginning of the study. Results acquired by both devices are shown in Table 1. ΔV is the increase (in percent) in skin hydration parameter 30 minutes/1 month later compared to the beginning of the study as the average for all 39 participants, SE is standard error.

Table 4. Results of the change in skin hydration parameter of the short-term and long-term clinical study.

			NIR device	Two-sample T Test		*DermaLab*	Two-sample T Test
Short-term study	Control	ΔV	**+1,4%**	NO statistically significant difference	ΔV	**-5%**	Statistically significant difference
		SE	0,7%		SE	1%	
	Cream	ΔV	**+4,5%**	Statistically significant difference	ΔV	**+7%**	Statistically significant difference
		SE	0,6%		SE	1%	
Long-term study	Control	ΔV	**+2,3%**	Statistically significant difference	ΔV	**+32%**	Statistically significant difference
		SE	0,6%		SE	5%	
	Cream	ΔV	**+1,9%**	Statistically significant difference	ΔV	**+78%**	Statistically significant difference
		SE	0,7%		SE	13%	

The NIR device was developed in such a way to decrease the measurement depth as much as possible by arranging illumination and detection fibers without any separation between them. For analysis, only water absorption maximum of 1450 nm was used as it highly absorbs water, thus decreasing the penetration depth. For future studies, cross polarizers might be incorporated in the experimental setup to reduce specular reflectance off the skin surface. Also, it might be useful to use illumination and detection fibers of a lower diameter (in this study, fibers of 400 μm in diameter were used), thus possibly reducing the penetration depth even more.

Unfortunately, there is no "golden standard" method to estimate skin hydration and compare results of our developed device to. Even though there are different commercially available devices for estimation of skin hydration based on electrical properties of skin (conductance, capacitance), we believe that optical methods might be useful and maybe even better for this purpose as they can work in a non-contact mode (e.g. NIR imaging) providing less effect of skin surface nonuniformity and roughness, dependence on contact pressure on skin surface, compared to devices based on electrical properties of skin. During the measurements by *DermaLab* device, we noticed that the results vary quite a lot when doing a measurement at approximately the same spot of forearm skin within a short period (less than half a minute). In some test measurements, the standard deviation between 5 measurements on the same spot was close to 20%. For NIR device, it was normally less than 2%. We also noticed another issue regarding measurements by *DermaLab* device – for a couple of participants, skin hydration measurement 1 month later showed an increase of up to 10 times, compared to the beginning of the study, which seemed a very unlikely result. We considered these results as faulty and did not include them in the calculation of the average value. The reason might be the use of some specific chemical substances on skin that systems based on conductance measurements are very sensitive to, even though none of the participants could recall being exposed to anything unusual.

Overall, we conclude that *DermaLab* is more sensitive to small changes in skin hydration, compared to our developed NIR device. One of the reasons might be the deeper measurement depth by NIR spectroscopy device. There is currently no standardized method for NIR spectroscopy application for estimation of skin hydration, thus more research in this field is needed.

4. Clinical validation of the skin multimodal imaging prototype device „SkImager".

Rosacea is a chronic inflammatory skin disease that involves flushing, transient or persistent erythema, visible blood vessels (*telangiectasias*), as well as papules and pustules on central convexities of the facial skin (cheeks, chin, nose, and central forehead). These are considered the primary features of *rosacea*. It is one of the most common conditions that dermatologists treat with a prevalence of 2-22% in Europe. Pathophysiology of *rosacea* is not fully understood and involves dysregulation of several systems, including innate immunity and neurovascular mechanisms, and the cause of *rosacea* is still being discussed. Its severity is usually determined clinically by visual assessment of primary features of *rosacea*, including erythema. Different scales are used for erythema assessment in clinical trials, and up until now there has been no validated scale for erythema estimation. Recently, a relatively reliable Clinician's Erythema Assessment (CEA) grading scale has been introduced that ranges from 0 (clear skin, no erythema) to 4 (severe erythema). The accuracy of the measurements is of great importance as it is often used as the golden standard for evaluation of *rosacea* treatment cream performance. Unfortunately, it is impossible to avoid evaluator bias.

(a)

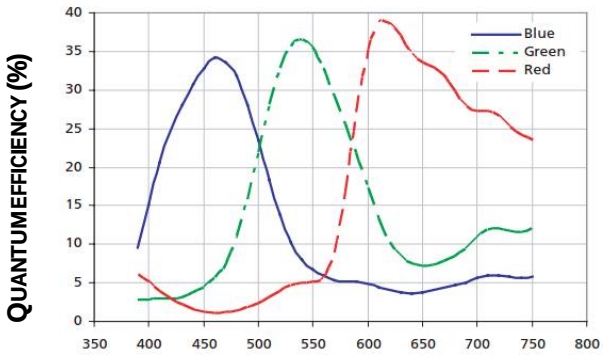

(b)

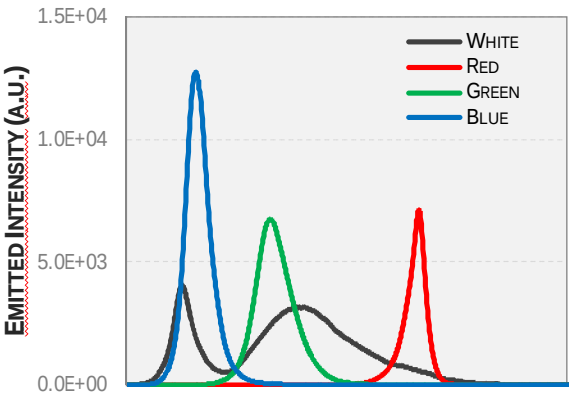

(c)

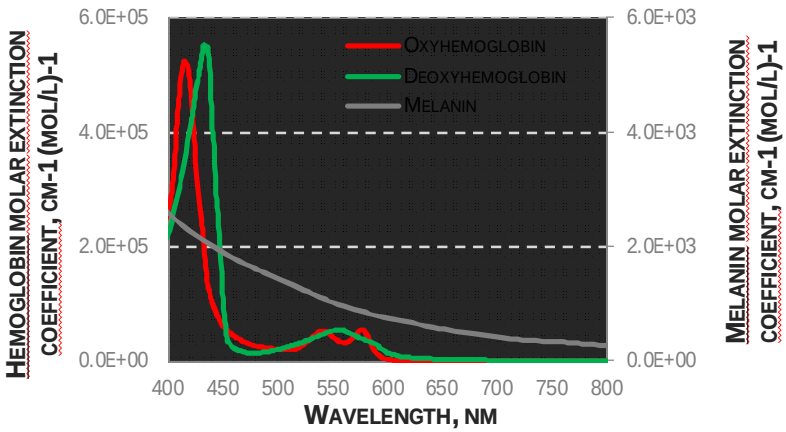

(d)

Fig.36. (a) Quantum efficiency of the CMOS sensor used in SkImager, (b) Spectra of SkImager LEDs, (c) Skin chromophore absorption spectra, (d) A photo of the experimental RGB imaging device SkImager.

More objective erythema estimation can be done by spectroscopic devices (e.g., *Mexameter*®, *Chromameter*®, *DermaSpectrometer*®), computer analysis of a digital photograph, lesion counts of papules and pustules, and assessment of secondary signs and symptoms (burning, stinging, itching). Studies show possibilities to distinguish *rosacea* from other common facial inflammatory skin diseases involving erythema, such as seborrheic dermatitis, discoid lupus erythematosus and granulomatous skin diseases, by dermoscopic patterns (e.g. dotted vessels, orange-yellowish areas, pigmentation structures). Computer-aided image analysis has been shown to be useful for differentiation between facial erythematous diseases such as *rosacea* and seborrheic dermatitis which is often mistreated by the visual inspection of dermatologists.

The experimental RGB imaging prototype with provisional brand name *SkImager* is a handheld wireless, battery-powered device. It comprises a 3 Mpix CMOS sensor color camera (*Micron* MT9T031, quantum efficiency shown in figure 36a, surrounded by a ring-shaped LED illuminator, linear polarizers in front of the LEDs and the camera, oriented orthogonally to each other to suppress the specular reflection an on-chip microcomputer, a touchscreen and an SD memory card. The LED ring can emit at white, blue (460 nm), green (530 nm), red (665 nm), infrared (940 nm) and UV (375 nm) spectral bands; only white, blue, green and red bands were used in this study (figure 36b). The distance between skin surface and the detector is kept constant at 50 mm and the device touches skin surface so that outside light does not reach the detector. Skin area of 30 mm in diameter can be evaluated. Illumination LEDs are evenly distributed in a circle, and each type of LEDs is sequentially switched on for approximately 1 second while an RGB image is taken, thus the total measurement time is approximately 5 seconds. A photo of the experimental device *SkImager* in its stand is shown in figure 36d.

Mexameter® is a commercially available device that comprises 16 circularly arranged LEDs emitting at wavelengths 568 nm (green), 660 nm (red) and 880 nm (near-infrared), and a photodetector that measures intensity of the light reflected by skin area of 5 mm in diameter. Erythema index is calculated from reflected light intensities at 568 nm and 660 nm LED illumination. *Mexameter*® can also estimate melanin index by using reflected light intensities at 660 nm and 880 nm LED illumination.

The most available and commonly used devices by dermatologists (e.g. *Mexameter*®) estimate only a small region of skin (around 5 mm in diameter) by a single photodetector that does not allow a simple and reliable estimation of skin erythema of a larger region of skin. It is very important to develop a simple and reliable method for skin erythema estimation of a larger area of skin, as local factors such as *telangiectasia* may influence the result substantially, and RGB imaging is a promising tool to achieve that. Thus, the objectives of this study were the following: (1) to compare a new RGB based imaging system to sample a larger skin area (30 mm in diameter), the prototype *SkImager*, with a commonly used point measurement device *Mexameter*® for the evaluation of *rosacea*, (2) to evaluate a new image processing method using only two adjacent spectral channels, (3) to evaluate and compare various in the literature available erythema index estimation algorithms, including the one proposed in this study, and (4) to compare the objective measurements, acquired by *Mexameter*® and *SkImager* to clinicians' assessment using the CEA scale. This study suggests new methods and algorithms for estimation of skin erythema, provides results on how well the two optical methods correlate with clinicians' subjective assessment, thus adding new insights to the current literature on estimation of facial skin erythema.

Absorption spectra of skin chromophores oxyhemoglobin, deoxyhemoglobin and melanin are shown in figure 31c. The most spectroscopic techniques for erythema assessment are mainly based on comparison of diffuse reflected intensities at different spectral bands - mostly green and red, due to high hemoglobin absorption in the green spectral region and very low absorption in the red. Erythema index can then be calculated as:

$$EI_{RG} = log\frac{I(R)}{I(G)} \approx \frac{I(R)}{I(G)} \quad (9)$$

where $I(R)$ is reflected intensity of the red light and $I(G)$ is the reflected intensity of the green light. For RGB imaging purposes, logarithm in the formula is often neglected, as only relative values are further used. The approximately equal sign in (1) is used to show that the important parameter here is the ratio between the two signals that describe absorption of hemoglobin. In this study, only the ratio (not the logarithm of the ratio) was further used, as only relative parameter values are observed. Although there is even higher hemoglobin absorption in the blue spectral range, it is not commonly used due to lower mean penetration depth in skin (less than 300 µm compared to approximately 500-700 µm for the green light).

This study analyzed three data sets: visual assessment by two dermatologists (CEA, scale from 1 to 4), *Mexameter® MX18* measured erythema index value (EI_M, scale from 1 to 1000), and four erythema index values based on the RGB imaging device measurements and calculated by using four different erythema index estimation algorithms - $EI_{RG}, EI_{BC}, EI_{BRG}$ and a newly proposed erythema index estimation EI_{BG} that will be explained shortly.

SkImager acquires one RGB image at each illumination (red, green and blue LEDs). Each of the three RGB images can be separated into three spectral images (red, green and blue), thus obtaining nine images in total. Each spectral image represents three roughly separated spectral regions: 600-700 nm (red), 500-600 nm (green), and 400-500 nm (blue) (figure 1a). For each illumination only one spectral image was further used: red spectral image for red LED illumination, green spectral image for green LED illumination, and blue spectral image for blue LED illumination. Each pixel provided the reflected intensity value at red, green and blue illumination: $I_i(R)$, $I_i(G)$ and $I_i(B)$, respectively.

A new parameter was introduced for erythema severity estimation. The reason for this was to improve the already introduced melanin-corrected algorithm by modifying it so that only two adjacent spectral band images are used for erythema index calculation. The algorithm was found empirically by taking into account the following considerations. Hemoglobin absorption can be related to difference between the red and the green spectral images, however, melanin absorption in the upper skin layers should also be considered. Erythema index can be estimated as absorption in green spectral band, melanin absorption can be related to difference in absorption between blue and green spectral bands, and thus melanin-corrected erythema index can then be estimated as:

$$\mathrm{EI_{BG}} = \mathrm{OD(G)} - [\mathrm{OD(B)} - \mathrm{OD(G)}] \quad (10)$$

or:

$$\mathrm{EI_{BG}} = \log\left[\frac{[I_0(G)]^2}{I_0(B)} \cdot \frac{I(B)}{[I(G)]^2}\right] \approx \frac{I(B)}{[I(G)]^2} \quad (11)$$

as the first multiplier in the formula is a constant for all measurements. Further a multiplier of 100 is used for better data representation:

$$\mathrm{EI_{BG}} = 100 \cdot \frac{I(B)}{[I(G)]^2} \quad (12)$$

Erythema index for each measurement is calculated as the mean erythema index value of all pixels of the skin area of interest.

The study protocol was approved by the local ethics committee, and each patient gave a written informed consent before the trial. This study only focused on *rosacea* patients. All patients had Fitzpatrick skin types I or II. In order to distinguish erythema caused by rosacea and erythema potentially caused by another etiology, a primary screening procedure was done by a dermatologist. Only patients with *erythematotelangiectatic rosacea* subtype were enrolled in this study. Differential diagnoses to be ruled out included seborrheic dermatitis, allergic and irritant contact dermatitis and connective tissue diseases such as systemic lupus erythematosus.

Five parts of facial skin were measured for each patient (central forehead, right cheek, left cheek, right part of nose and left part of nose). Most measured areas 30 mm in diameter involved both visibly seen blood vessels and some regions of normal skin without any visible erythema, except in some cases with a more severe *rosacea* where the whole imaging area was erythema. For each facial part three data sets were obtained: adopted CEA, *Mexameter*® erythema index values (EI_M), and *SkImager* erythema index values ($EI_{RG}, EI_{BC}, EI_{BRG}, EI_{BG}$). Before each measurement, patient was asked to sit still and relax for at least 15 minutes in order to avoid other factors affecting their skin color (such as cold outside temperature, fast walking, etc.). Two dermatologists independently graded persistent erythema on each of the five facial regions on a 4-point scale (1 – mild, 2 – moderate, 3 – severe, 4 – very severe erythema), and for all 50 patients their opinions matched. 50 female *rosacea* patients (ages 25 to 60) with dermatologists' estimated CEA index participated in the study. Two sets of follow-up measurements for each patient were performed one month apart.

The obtained results are presented in two parts: comparison between different erythema index estimation algorithms, including the newly proposed algorithm, and comparison of results of all three data sets (CEA, *Mexameter*® and *SkImager*) for 500 measurements (50 patients, twice measured, 5 facial regions).

Comparison of different erythema index estimation algorithms

It was expected that visibly seen blood vessels and other regions with an increased redness would result in increased erythema index values, compared to normal skin. As most of the acquired data included skin regions of both visibly seen blood vessels and areas of normal skin, an analysis was done to compare different erythema index estimation algorithms and see which calculation gives the best contrast between areas of increased redness and normal skin, and which one gives the best contrast between areas of pigmentation (increased melanin absorption) and normal skin. Data of only those patients who had visibly seen blood vessels, visibly seen pigmented areas and visibly seen areas of normal skin in the same region of 30 mm in diameter were used, to be able to segment between those three areas and compare the average erythema index of each of the three areas. For this analysis, only 30 (out of 50) patient data were used, as most of the others did not have distinguishable areas between blood vessels, pigmented areas and normal skin. This analysis was done by looking at a white LED illumination image and manually, by visual inspection selecting three separate areas on any part of patient's facial skin (either forehead, noise or cheek): a region of visibly normal skin, a region of increased redness (i.e. visibly seen blood vessels) and a region of pigmentation (increased melanin content). The manually chosen area of normal skin can possibly also be with a little higher erythema index than non-facial skin (e.g. area close to ear) as it was taken from a relatively small area of 30 mm in diameter, some part of which is increased erythema, e.g. blood vessels. However, this analysis was only done to compare different erythema index calculations, and the same areas were chosen for all four different calculations. Thus, even if the chosen area of normal skin included an area of increased erythema, there is still visibly seen contrast between this chosen normal skin and visibly seen blood vessels which have much higher erythema index value than the normal skin.

Example of one of the data used is shown in figure 32. In the upper row, white LED illumination RGB image, blue LED illumination blue spectral channel, green LED illumination green spectral channel and red LED illumination red spectral channel images are shown; in the lower row normalized erythema index maps are shown, representing each of the four used calculations for erythema index estimation. We can observe from the white LED illumination image that there are visibly seen blood vessels and an area around them with an increased redness, compared to the areas that appear as normal skin. We can also observe pigmentation – little brownish dots throughout the whole image area, including that of increased erythema. When looking at the four different erythema index distribution maps which are all normalized from 0 to 1, we can observe some similarities: the visibly seen blood vessels seem to be with the highest erythema index value for all erythema index estimations. However, for EI_{RG} and EI_{BC} (lower left images of figure 32), the pigmented dots seem to be much more distinguishable than for EI_{BRG} and EI_{BG} which can be expected, as the first two calculations do not correct for melanin absorption, thus pigmented dots can also be perceived as increased erythema. By visible inspection of all erythema index distribution maps, EI_{BG} map seems to

show the best contrast between blood vessels and normal skin around them. EI_{BC} seems to appear a bit blurrier in terms of contrast between the blood vessels and the surrounding areas. However, any of these erythema index distribution maps could be of a great help for a clinician to determine areas of increased erythema as in some cases they could be too small or too low in contrast to observe by visual inspection.

In the white LED illumination image three small regions of interest of at least 10 pixels each were chosen: one representing a region of normal skin (black ROI line in figure 2 white image), one representing a region of increased redness (red ROI line in figure 37 white image) and one representing pigmentation (blue ROI line in figure 37 white image). The average erythema index value of each of the three regions, as well as the standard deviation was then calculated, and it was done for all four erythema index calculations for comparison. To estimate the contrast between increased erythema and normal skin, the average erythema index value of a region of increased redness was divided by erythema index value of a region of normal skin. Similarly, the contrast of pigmentation and normal skin was calculated by dividing the average erythema index value of pigmentation with the average erythema index value of normal skin. An example of the calculated contrast parameters of one patient is shown in table 5.

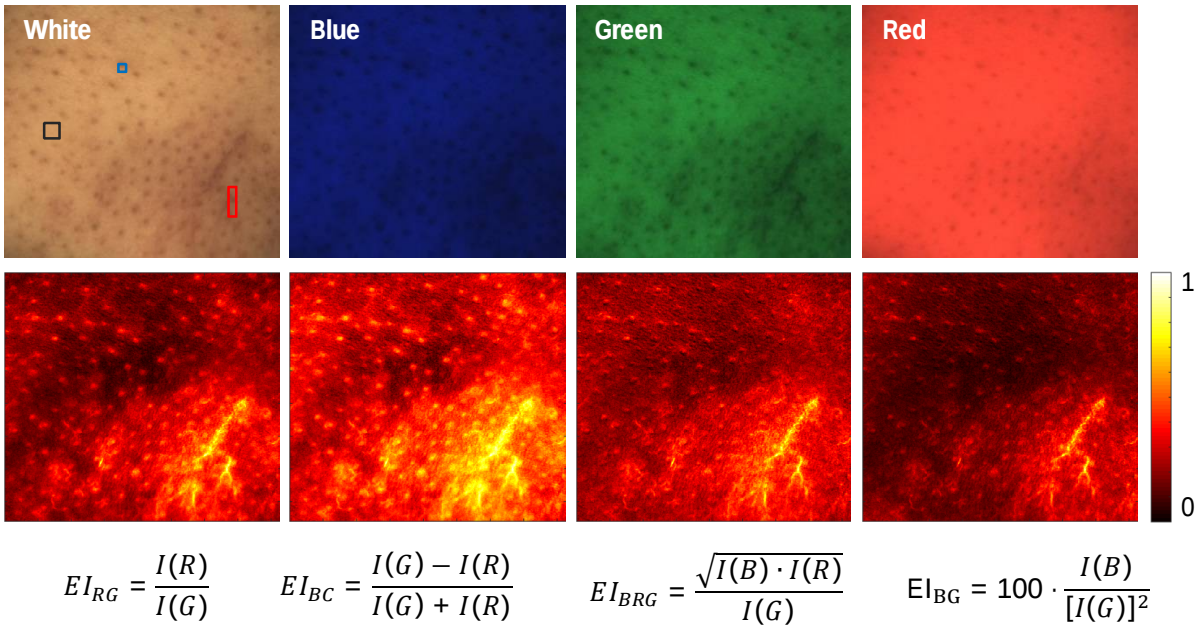

Fig. 37. Example of acquired and analyzed data of a nose of a female patient (skin type II); upper row: white illumination RGB image and blue, green and red LED illumination spectral images; lower row: normalized erythema index distribution maps of all four different calculations.

Out of all the analyzed 30 patient data, for each patient the maximum contrast of blood vessels and normal skin and contrast of pigmentation and normal skin value was estimated to determine which erythema index calculation gives the best contrast. In case of contrast of blood vessels and normal skin, it is better to have a higher contrast value as it increases the scale of the level of redness that can be distinguished. In case of contrast of pigmentation and normal skin the lowest contrast value is the best as it means that the absorption of melanin has been subtracted more.

The best contrast between an increased erythema (blood vessels) and normal skin was achieved by using the EI_{BG} estimation algorithm (the highest contrast value for 29 out of 30 patients) (table 2). For 1 of 30 the highest contrast value was shown by the EI_{BC} algorithm. In case of contrast between pigmentation and normal skin the lowest contrast value was achieved using the EI_{BRG} estimation algorithm (the lowest contrast value for 27 out of 30 patients). For 3 out of 30 patients the lowest contrast value was shown by the EI_{BC} algorithm.

By analyzing results of 30 patient data, the erythema index ranges were estimated for normal skin, increased erythema and pigmentation. For EI_{BG} estimation algorithm, erythema index values for normal skin ranged from 0.09 – 1.27 with an average of 0.77; for skin area of increased erythema (e.g. blood vessels) the values ranged from 0.86 – 3.69 with an average of 1.76; for skin area of pigmentation (increased melanin content) the values ranged from 0.48 – 3.24 with an average of 1.28. Some ranges overlap which can be explained by the fact that the selection of the three regions of interest (normal skin, blood vessels and pigmentation) was done manually, by visual inspection and separately for each patient data. Thus, what for some patient data was observed as reduced redness (normal skin), for others was increased redness, compared to the surrounding skin area. To obtain more accurate erythema index value ranges for normal skin, the area of normal skin should be imaged at some other location, possibly even non-facial, e.g. the area of an ear.

Table 5. Example of the calculated contrast parameters of one patient data.

	Normal skin	**Blood vessels** (increased erythema)	**Pigmentation** (increased melanin content)	**Contrast of Blood vessels and Normal skin**	**Contrast of Pigmentation and Normal skin**
$\boldsymbol{EI_{RG}}$	0.11 ± 0.01	0.91 ± 0.05	0.61 ± 0.12	8.27 ± 0.43	5.55 ± 0.70
$\boldsymbol{EI_{BC}}$	0.18 ± 0.02	0.95 ± 0.03	0.75 ± 0.10	5.28 ± 0.16	4.17 ± 0.41
$\boldsymbol{EI_{BRG}}$	0.17 ± 0.02	0.90 ± 0.05	0.58 ± 0.13	5.29 ± 0.31	3.41 ± 0.45
$\boldsymbol{EI_{BG}}$	0.09 ± 0.01	0.89 ± 0.06	0.48 ± 0.13	9.89 ± 0.67	5.33 ± 0.72

Comparison of CEA, Mexameter and SkImager results

For 500 total measurements, three data sets were analysed: CEA, *Mexameter*® and *SkImager* erythema estimation values. All 500 measurements were divided in four groups, depending on the corresponding CEA value of each measurement, and boxplots, created with *Matlab*, show the correlation of CEA and EI_M values, acquired by *Mexameter*® (figure 38). The box in the plot represents all data of 25th to 75th percentiles; the lines include 99.3% of all the data, and the red crosses represent outliners. The blue dots in the box represent the medians, and linear fitting of medians and CEA values was done to acquire the coefficient of determination R^2.

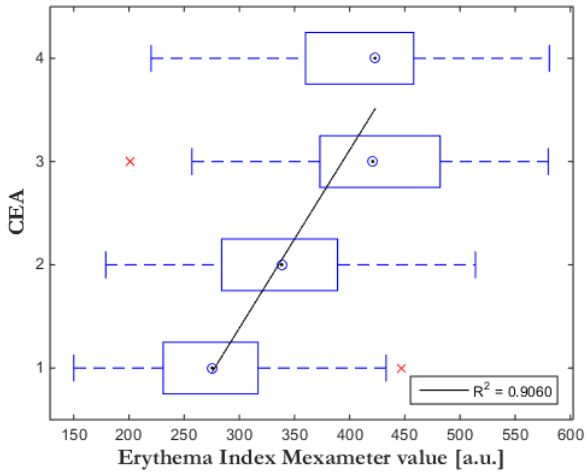

Fig. 38. A boxplot of all Mexameter® estimated erythema index $\boldsymbol{EI_M}$ values for each corresponding CEA value and linear regression correlation between CEA value and the median value of $\boldsymbol{EI_M}$ for each corresponding CEA value.

Similarly, boxplots of two of the erythema index estimation algorithms EI_{BRG} and EI_{BG} are shown in figure 39. The correlation graphs clearly show a much better linear correlation (R^2~0.99) between CEA and the median EI_{BRG} and EI_{BG} values. Correlation between CEA and the other two erythema index estimation algorithms (EI_{BC} and EI_{RG}) was also calculated, and the coefficients of determination are R^2 = 0.99 for both. It seems that there is not much difference when comparing all four different erythema index estimation algorithms in terms of how well they correlate with dermatologists' estimated CEA, however they show a much better correlation when comparing with erythema index estimations acquired by *Mexameter*®.

Linear fitting was also done on all data points (not just medians) to see how well all the CEA and EI values correlate. As expected, the coefficients of determination are not very high. The lowest coefficient value is for EI_M (R^2 = 0.30). The other four erythema index estimation algorithms show similar coefficient values: R^2 = 0.44 (EI_{RG}), R^2 = 0.44 (EI_{BC}), R^2 = 0.45 (EI_{BRG}) and R^2 = 0.44 (EI_{BG}).

A statistical analysis on all calculated erythema index data was performed to test how well different CEA groups can be distinguished between each other, based on their respective EI values. In this case, each CEA estimation by the clinician was considered as an independent variable, and also each EI measurement by both devices was considered an independent variables. Thus, a two-sample t-test was performed to test whether there is a significant (p < 0.05) difference between two consecutive CEA groups (1 and 2, 2 and 3, 3 and 4) for all EI estimation algorithms. Results show that there is a significant difference (p < 0.05) between the groups for all EI estimation algorithms except EI_M results, acquired by *Mexameter*® – there was not a significant difference between CEA groups 3 and 4 for EI_M.

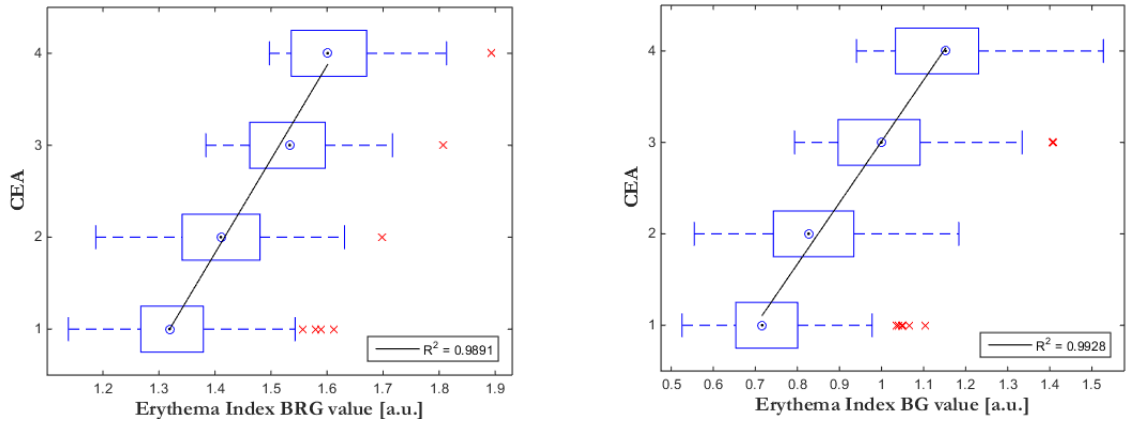

Fig. 39. Boxplots and correlation graphs between CEA and $\boldsymbol{EI}$ for all four $\boldsymbol{EI}$ estimation algorithms.

In conclusion, this study showed that single-spot measurements might not be very reliable when compared to the RGB imaging even though they are often used in clinical studies. RGB imaging shows a much better correlation with dermatologists' estimation and provides more reliable results. A new erythema index estimation algorithm was proposed, and it demonstrates a better contrast between blood vessel and normal skin regions than the other, previously proposed algorithms.

The above-described study was continued in order to develop software that allows to download the R, G and B images and to select the region of interest on the RGB image where segmentation maps are calculated. Principal component analysis is a statistical technique widely used in different areas for extracting the largest possible variance among the large datasets. This method showed good results in multispectral image analysis for diagnostics of pigmented skin lesions. The first and second principal components were recognized as useful for a melanoma and benign nevi differentiation in these studies. Otsu's segmentation is a method that uses histogram of an image to find the optimal threshold by maximizing between-class variance. This is one of the methods that are used for an automatic image segmentation of different skin lesions. This study compares the principal component analysis and

erythema index combined with multilevel Otsu's segmentation to evaluate the application possibilities for rosacea lesions therapy monitoring.

We used RGB images of rosacea lesions that were acquired by *SkImager*. From the previous study 10 cases with a diagnosis CEA = 1, 2 and 3 were processed and analyzed. The images of 6 rosacea patients with diagnosis CEA=2 before therapy (first visit) and CEA=1 approximately one month after treatment (second visit) were compared. A set of images from a forehead, both cheeks and both nose parts were available. In this study only the images from forehead and both cheeks were analyzed to exclude the impact of shadows on the calculated maps that appeared on curved areas of the nose.

A diagram of an image processing algorithm is shown in the figure 40. The RGB images were used for calculation and segmentation of erythema index and principal component maps. Image processing was performed in MatLab®. For analysis a region of interest (14x15mm) was taken manually from measured skin image. Three components of PCA were estimated from RGB image. The erythema index map was calculated by dividing red with green images: EI=R/G. To enhance skin vascular structures, segmentation of the maps was performed using multilevel thresholding by Otsu's method. The areas of the segmented regions were calculated as a percentage of the region of interest, analyzed and compared. Mean values of each cluster of 6 cases with the same CEA were analyzed before and after treatment.

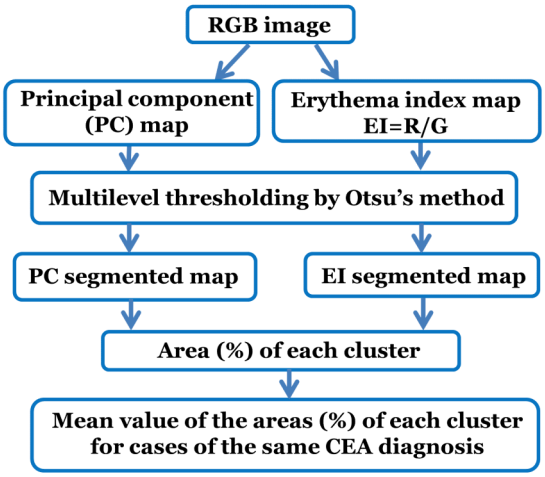

Fig. 40. Scheme of the image processing algorithm.

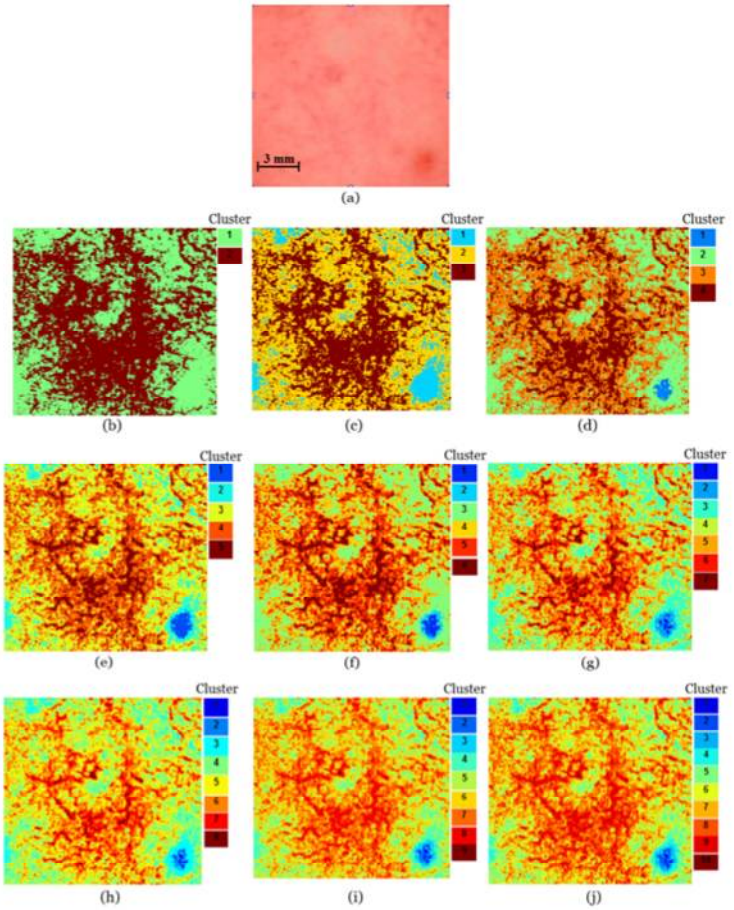

Fig. 41. RGB image (a) and segmented maps of erythema index (b-j) from a right cheek of a patient with a diagnosis CEA =3. Clusters are displayed in jet scale, maps are segmented in different numbers of clusters started from two (b) to ten (j).

Figure 41 shows an example of an RGB image and segmented EI maps with different segmentation clusters (from 2 to 10) from the right cheek of a patient with diagnosis CEA=3. In the figures with the number of clusters less than 5 the visible blood vessels and areas of erythema visually are not segmented precisely: the cluster with the highest order number occupies larger area than visible blood vessels on the RGB image. After analysis of some segmented maps we decided that segmentation in 5 clusters is sufficiently precise for initial lesions' area assessment. However, in the future, the analysis of the clusters' number influence on the results should be done.

Since we did not observe significant patterns for lesions' assessment on the maps of the second principal component further only the PC1, PC3 and EI maps will be discussed. Examples of RGB images and segmented maps of five clusters are shown in figure 42.

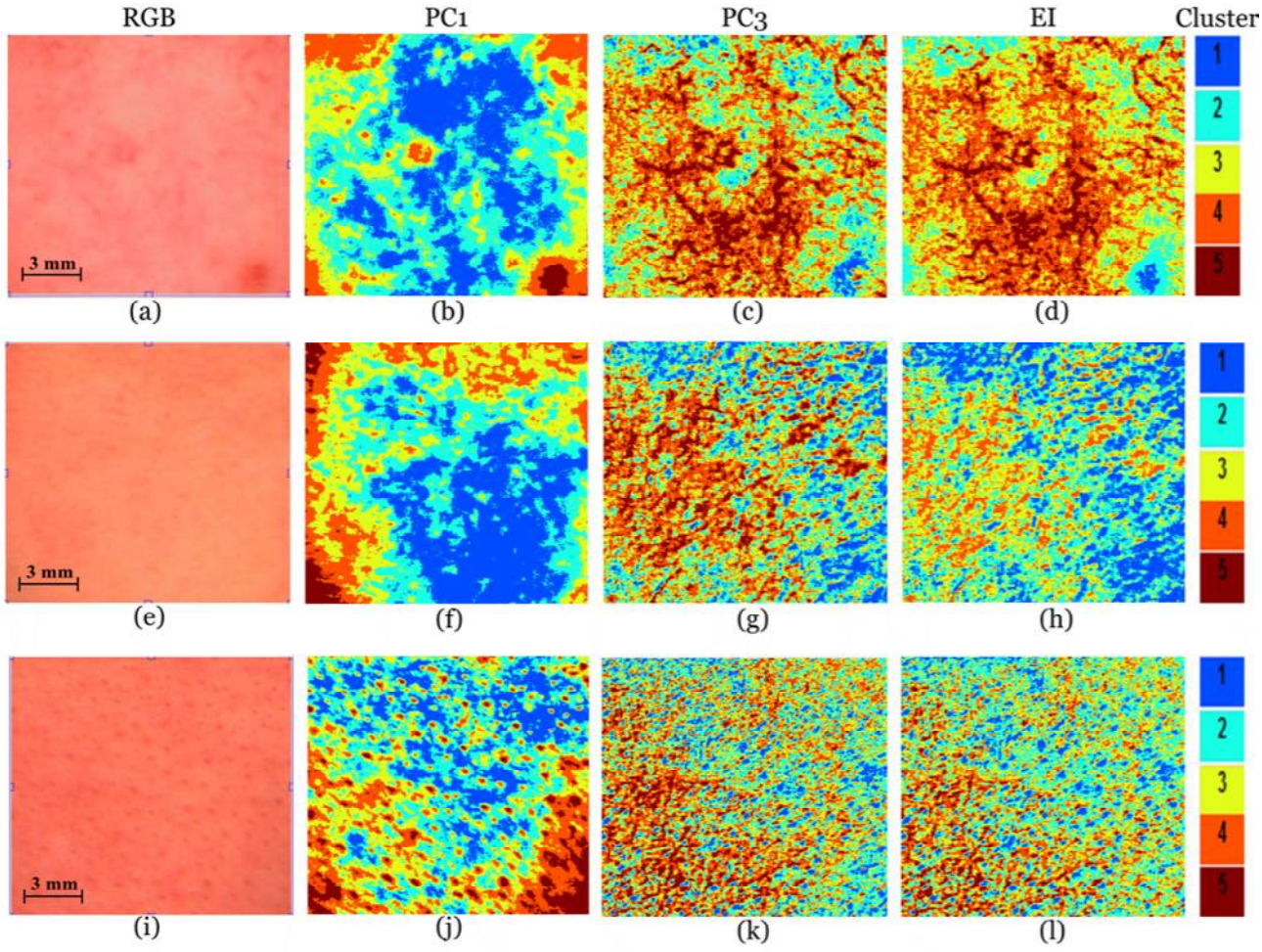

Fig. 42. RGB images (a, e, i) and segmented maps of the first principal component – PC1 (b, f, j), the third principal component – PC3 (c, g, k) and erythema index – EI (d, h, l) from a right cheek of a patient with a diagnosis CEA = 3 (a – d), a left cheek of a patient with a diagnosis CEA = 2 (e – h), and a forehead of a patient with a diagnosis CEA = 3 (i – l). Five clusters are displayed in jet scale: blue color corresponds to the first cluster, brown color – to the fifth cluster.

Figure 42 (a–d) shows RGB image and segmented maps of a right cheek for a patient with a diagnosis CEA=3. The distribution of the clusters' areas on PC3 and EI segmented maps are very similar. The regions of the skin that visually appear white on the RGB image are segmented in the first cluster (blue color), but blood vessels and more red parts are segmented in the fifth cluster on all segmented maps. Pigmented part (in the right lower corner of the image) of the skin are segmented in the fifths and fourth clusters along with the blood vessels and erythema on PC1 map while on the PC3 and EI maps – in the first and second cluster. Similar patterns are observed on the maps of a left cheek for a patient with diagnosis CEA=2 (Fig.2 (e – g)).

Figure 42 (i – l) shows RGB image and segmented maps of a forehead for a patient with diagnosis CEA=3. In this case the algorithm segments skin pores in the fifth cluster on PC1 map along with shadows in the corners of the image, but on the PC3 and EI maps in the opposite (the first) cluster.

Figure 43 shows the mean values of clusters' areas on EI and PC3 maps of 6 rosacea patients who had diagnosis CEA=2 on the first visit and CEA=1 on the second visit. The mean values of the first and second clusters that correspond to whiter/healthier skin parts increase after the therapy, but the values of the fifth and forth (blood vessels/erythema) decrease on both EI and PC3 maps. Although standard deviations (SD) of the mean values are large and there is an overlap of SD for the values obtained before and after therapy, the results are in line with the doctor's assessment.

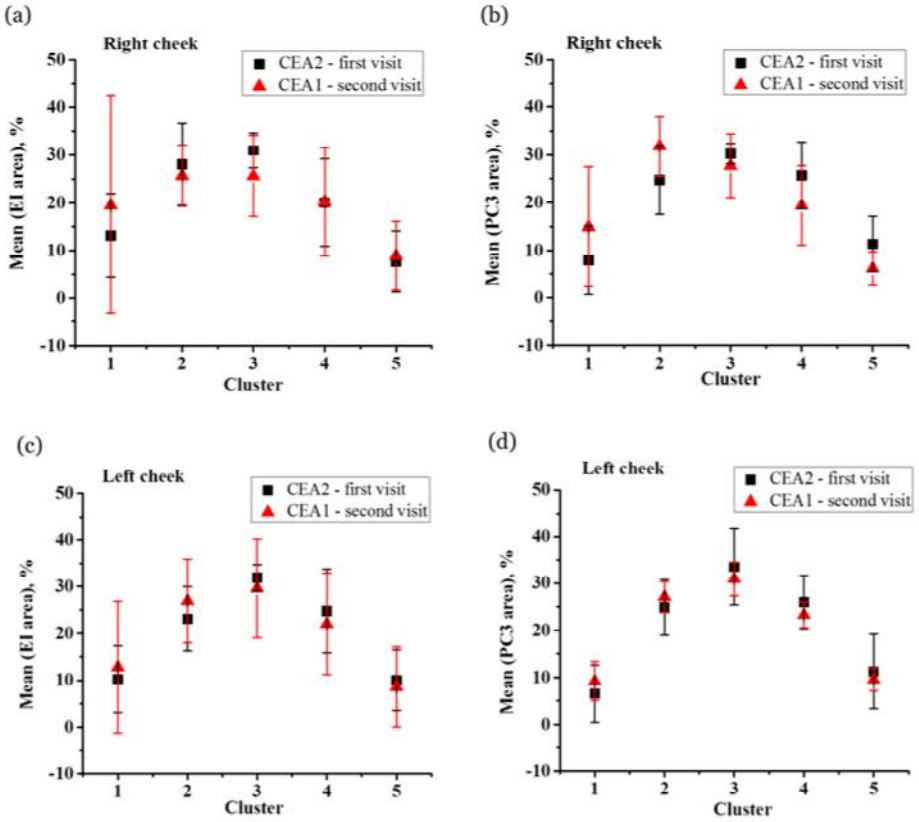

Fig. 43. Mean values of clusters' areas of EI (a, c) and PC3 (b, d) segmented maps on a left and right cheek of 6 rosacea cases which have been diagnosed as CEA=2 on the first visit, and CEA=1 on the second visit. The first cluster corresponds to lighter skin colour, the fifth cluster – to reddish skin/erythema.

To conclude, the analysis of different numbers of segmentation levels showed that segmentation in 5 clusters is sufficiently precise for redness and blood vessels distinction and lesions' area assessment. Visible blood vessels are segmented more precisely on EI (erythema index) and PC3 (the third principal component) maps than on PC1 (the first principal component) maps. In many cases we found that the distribution of clusters on EI and PC3 maps are very similar. Skin pigmentation is segmented in the same cluster with the lighter skin parts on these maps which is opposite to the cluster where redness and blood vessels are segmented. Skin pigmentation, blood vessels and shadows are not distinguished and are segmented in the same cluster on PC1 maps. Mean values of clusters' areas on EI and PC3 maps show the decrease of the area of blood vessels and erythema and the increase of the lighter skin area after the therapy. These results are in line with the doctor's assessment: the diagnosis on the first visit was CEA = 2, on the second visit (after therapy) - CEA=1. In summary, this study shows that EI and PC3 maps are more useful than PC1 and PC2 maps for indicating vascular structures and erythema on the skin of rosacea patients and therapy monitoring.

Conclusions

To summarize, the planned goals and tasks of the project have been achieved and in some positions also surpassed. The original imaging technologies are approbated in laboratory and clinical environment; their applicability for non-contact mapping of skin pathology and microcirculation parameters has been confirmed. Results are significant for clinical diagnostics and monitoring, as objective quantitative information about the health state can be obtained in a patient-friendly manner. The scientific significance of results is determined by novelty of the developed technologies, confirmed by 4 patent applications, 16 international level publications and 26 conference reports presented at 10 countries worldwide. Results of the project are practically implemented at the Riga Hospital of Traumatology and Orthopaedics (remote control of anaesthesia efficiency during surgeries) and at Latvian Oncology Centre, RAKUS (non-contact diagnostics of skin tumours).

References: publicity of the results

Papers in journals with SNIP>1

1. I.Saknite, A.Zavorins, D.Jakovels, J.Spigulis, J.Kisis, "Comparison of single-spot technique and RGB imaging for erythema index estimation", Physiol. Meas. 37(3), 333-346 (2016). SNIP = 1.09.
2. J.Spigulis, I.Oshina, A.Berzina, A.Bykov, "Smartphone snapshot mapping of skin chromophores under triple-wavelength laser illumination," J. Biomed. Opt. 22(9), 091508 (2017). SNIP = 1.20.
3. J.Spigulis, "Multispectral, fluorescent and photoplethysmographic imaging for remote skin assessment", Sensors 17(5), 1165 (2017). SNIP = 1.39.
4. A.Lihachev, I.Lihacova, E.V.Plorina, M.Lange, A.Derjabo, J.Spigulis, "Differentiation of seborrheic keratosis from basal cell carcinoma, nevi and melanoma by RGB autofluorescence imaging", *Biomed.Opt.Expr.* (submitted 2017). SNIP = 1.53.

Other SCOPUS-cited papers

1. J.Spigulis, I.Oshina, "3x3 Technique for RGB Snapshot Mapping of Skin Chromophores", *OSA Bio-Optics: Design and Applications 2015,* OSA Technical Digest (online 10.1364/BODA.2015.JT3A.39), Vancouver, CA (2015).
2. I.Saknite, A.Zavorins, J.Spigulis, J.Kisis, "Skin Erythema Assessment by an RGB Imaging Device: a Clinical Study", *OSA Frontiers in Optics 2015,* OSA Technical Digest (online https://www.osapublishing.org/abstract.cfm?uri=FiO-2015-JTu4A.16) , San Jose, USA (2015).
3. J. Spigulis, I. Oshina, Z. Rupenheits, "Smartphone single-snapshot mapping of skin chromophores," OSA *Biomedical Optics 2016*, OSA Technical Digest (online https://www.osapublishing.org/abstract.cfm?uri=Cancer-2016-JTu3A.46), Hollywood, USA (2016).
4. E.Kviesis-Kipge, U.Rubins, „Portable remote photoplethysmography device for monitoring of blood volume changes with high temporal resolution", *Proc. BEC2016*, 55-58, Tallinn, EE (2016).
5. U.Rubins, J.Spigulis, A.Miscuks, "Photoplethysmography imaging algorithm for continuous monitoring of regional anesthesia", *ESTIMedia'16 Proceedings of the 14th ACM/IEEE Symposium on Embedded Systems for Real-Time Multimedia*, 67-71 (2016).
6. I.Saknite, A.Zavorins, I.Zablocka, J.Kisis, J.Spigulis "Comparison of a near-infrared reflectance spectroscopy system and skin conductance measurements for in vivo estimation of skin hydration: a clinical study", *J.Biomed.Photon.& Engin.*, 3(1), http://jbpe.ssau.ru/index.php/JBPE/article/view/3166/3068, (2017).
7. U. Rubins, A. Miscuks , M. Lange, "Simple and convenient remote photoplethysmography system for monitoring regional anesthesia effectiveness". *Proc. IFMBE* **65**, 378-381 (2017).
8. J.Spigulis, «*In vivo* skin imaging prototypes "made in Latvia"», *Front. Optoelectron., 1-12* (2017).
9. I.Oshina, J.Spigulis, U.Rubins, E.Kviesis-Kipge, K.Lauberts, "Express RGB mapping of three to five skin chromophores", *Proc. SPIE-OSA* **10413**, 104130M-4 (2017).
10. U.Rubins, Z.Marcinkevics., «Comparison of remote photoplethysmography signals acquired by ultra-low noise camera and conventional camera during physiological tests", Proc. SPIE **10411**, 104110T (2017).
11. U.Rubins, A.Miscuks, Z.Marcinkevics, M.Lange. „Remote photoplethysmography system for unsupervised monitoring of regional anaesthesia effectiveness". *Proc.SPIE* **10592**, 1059203 (2017).
12. I.Kuzmina, U.Rubins, I.Saknite, J.Spigulis. „Rosacea assessment by erythema index and principal component analysis segmentation maps", *Proc.SPIE* **10592**, 1059204 (2017).
13. "Progress in Biomedical Optics and Imaging: Biophotonics Riga - 2017", SPIE Proceedings vol. 10592 (ed. Janis Spigulis), SPIE Press, Bellingham, USA (2017). ISBN: 9781510616769.

Patents and patent applications

1. LV 15106 B, 2016: J.Spigulis, I.Oshina. Method and device for mapping of chrompohores under illumination by several spectral lines.

2. LV P-17-17, 2017: U.Rubins, E.Kviesis-Kipge, J.Spigulis. Device for speckle-free imaging under scattered laser illumination.
3. PCT/EP2017/063565: U.Rubins, E.Kviesis-Kipge, J.Spigulis. Device for speckle-free imaging under laser illumination.
4. LV P-17-78, 2017: J.Spigulis, I.Oshina. Method for detection of colored counterfeits.

International conference presentations

1. J.Bauer, V.Heikkinen, J.Spigulis "Spectral reflectance estimation with an optical non contact device for skin assessment", *Northern Optics & Photonics 2015* (NOP 2015), Lappeenranta (FI), 2-4 June 2015.
2. I.Oshina, J.Spigulis, "Snapshot mapping of skin chromophores at triple-wavelength illumination" , 11th Int. Young Scientist Conference *Developments in Optics and Communications 2015*, Riga, 8-10 April 2015.
3. G.Tunens, I.Saknite, J.Spigulis, "Modeling diffuse reflectance spectrum of skin in the near-infrared spectral range by Monte Carlo simulations", 11th Int. Young Scientist Conference *Developments in Optics and Communications 2015*, Riga, 8-10 April 2015.
4. J.Bauer, V.Heikkinen, J.Spigulis, "Spectral reflectance estimation with an optical non contact device for skin assessment", 11th Int. Young Scientist Conference *Developments in Optics and Communications 2015*, Riga, 8-10 April 2015.
5. I.Oshina, J.Spigulis, "Image processing for snapshot RGB mapping of skin chromophores", Int.Conf. *IONS Karlsruhe 2015*, Karlsruhe (DE), 26-29 June 2015.
6. J.Spigulis, I.Oshina «Monochomatic spectral imaging: principles and application for skin chromophore mapping». *2nd Israeli Biophotonics Conference* (IBPC-2), 1-2 December 2015, Ramat-Gan (IL).
7. G.Tunens, I.Saknite, J.Spigulis. «Modelling skin diffuse reflectance spectra in the near-infrared and visible range», 12th Int. Young Scientist Conference *Developments in Optics and Communications 2016*, Riga, 21-23 March 2016.
8. R.Janovskis, I.Saknite, J.Spigulis. «Infrared spectroscopy and imaging for estimation of skin hydration». 12th Int. Young Scientist Conference *Developments in Optics and Communications 2016*, Riga, 21-23 March 2016.
9. I.Saknite, A.Zavorins, I.Zablocka, J.Spigulis, J.Kisis, "Comparison of Optical and Conductance Methods for Estimation of Skin Hydration", *Norwegian Electro-Optics Meeting 2016*, Voss (NO), 13-15 April 2016.
10. I.Saknite, A.Zavorins, I.Zablocka, J.Spigulis, J.Kisis,"Near-Infrared Reflectance Spectroscopy System for Noninvasive Estimation of Skin Hydration", *2nd Biomedical Imaging and Sensing Conference 2016*, Yokohama (JP), 17-20 May 2016.
11. J.Spigulis, "Multi-laser illumination designs for skin chromophore mapping". Int. Conf. *Advanced Laser Technologies (ALT16),* Galway (IE), 12-16 September 2016.
12. E.Kviesis-Kipge, U.Rubins, „Portable remote photoplethysmography device for monitoring of blood volume changes with high temporal resolution", *15th Bienn. Conf. on Electronics and Embedded Systems BEC 2016,* Tallinn (EE), 3-5 October 2016.
13. J.Spigulis, I.Oshina, Z.Rupenheits, "Smartphone single-snapshot mapping of skin chromophores", *OSA Biomedical Optics 2016*, Ft. Lauderdale (USA), 25-28 April 2016.
14. U.Rubins, J.Spigulis, A.Miscuks, "Photoplethysmography imaging algorithm for continuous monitoring of regional anesthesia", ESTIMedia'16, *14th ACM/IEEE Symp. on Embedded Systems for Real-Time Multimedia*, Pittsburgh (USA), 6-7 October 2016.
15. G.Tunens, I.Saknite, J.Spigulis, "Modelling skin diffuse reflectance spectra in the near-infrared spectral range", *SPIE BIOS'2017*, San Francisco (USA), 28 Jan-2 Feb 2017.
16. J.Spigulis, "Remote optical assessment of in-vivo skin: methods, prototype devices and clinical applications", *EMBEC'17 & NBC'17*, Tampere (FI), 11-15 June 2017.
17. M.Lange, U.Rubins, A.Miscuks, "Simple and convenient remote photoplethysmography (rPPG) system for monitoring regional anesthesia effectiveness", *EMBEC'17 & NBC'17*, Tampere (FI), 11-15 June 2017.
18. J.Spigulis "Hyperspectral and multispectral skin imaging", *Summer School on Optics & Photonics*, Oulu (FI), 1-3 June 2017.
19. E.V.Ploriņa, A.Lihachev, A.Derjabo, M.Lange *"Non-invasive evaluation of skin pathologies by RGB autofluorescence imaging"*, *Summer School on Optics & Photonics*, Oulu (FI), 1-3 June 2017.
20. I. Oshina, "Skin chromophore mapping and oxygen saturation measurements in human skin using polychromatic illumination", *Summer school "Biophotonics '17"* , Ven (SE),10-17 June 2017.

21. I.Oshina, J.Spigulis, U.Rubins, E.Kviesis-Kipge, K.Lauberts, "Express RGB mapping of three to five skin chromophores", *ECBO'2017,* Munich (DE), 26-29 June 2017.
22. U.Rubins, Z.Marcinkevics. «Comparison of remote photoplethysmography signals acquired by ultra-low noise camera and conventional camera during physiological tests», *ECBO'2017,* Munich, (DE), 26-29 June 2017.
23. I.Kuzmina, U.Rubins, I.Saknite, J.Spigulis. «Rosacea assessment by erythema index and principal component analysis segmentation maps», *Biophotonics Riga – 2017*, 27-29 August 2017.
24. U.Rubins, A.Miscuks, Z.Marcinkevics, M.Lange, «Remote photoplethysmography system for unsupervised monitoring of regional anaesthesia effectiveness», *Biophotonics Riga – 2017*, 27-29 August 2017 .
25. J.Spigulis, I.Oshina, «Multi-spectral-line imaging: applications in biophotonics and forensics», SFM Symposium *Optics and Biophotonics 2017*, Saratov (RU), 26-29 September 2017.
26. J.Spigulis, I.Oshina, "Monochromatic spectral imaging as a tool for counterfeit detection", *Int.Conf. "Forensics 2017"*, Caparica (PT), 19-23 November 2017.

Defended PhD Theses

1. Inga Saknite, "Optical non-invasive determination and mapping of skin bilirubin, hemoglobin and water" (supervisor Prof. J.Spigulis) – University of Latvia, 11.12.2015.
2. Vanesa Lukinsone, "Kinetics of in-vivo skin autofluorescence under continuous and pulsed laser excitation" (supervisor Prof. J.Spigulis) – University of Latvia, 12.12.2017.

Defended Master Thesis

1. Olga Ļashuka, „Determination of pulse wave velocity by the non-contact photoplethysmography method" (Supervisor Dr. Uldis Rubins.) – University of Latvia, 2015.
2. Jacob Bauer, "Spectral reflectance estimation with an optical non contact device for skin assessment" – University of Eastern Finland (Supervisors Prof. Ville Heikkinen and Prof. Janis Spigulis) – University of Eastern Finland, 2015.
3. Reinis Janovskis, "Infrared spectroscopy and imaging for assessment of skin hydration" (Supervisors Prof. Janis Spigulis and Dr. Inga SaknIte) – University of Latvia, 2016.
4. Ilze Oshina, "Mapping of skin chromophores under illumination by 3, 4 and 5 spectral lines" (Supervisor Prof. Janis Spigulis) – University of Latvia, 2017.
5. Antra Dzerve, "Skin fluorescence and scattering kinetics measurements at picosecond laser excitation (Supervisor Prof. Janis Spigulis) – University of Latvia, 2017.
6. Gatis Tunens "Modelling of optical radiation propagation in healthy and pathologic skin" (Supervisor Prof. Janis Spigulis) – University of Latvia, 2017.

PI of the project #3:

Janis Spigulis

Riga, 12/01/2018